Investigation of a Crystal Calorimeter Technology with longitudinal Segmentation

Diplomarbeit
zur Erlangung des akademischen Grades
Diplom-Physiker

eingereicht von

Ralph Dollan
geboren am 28. Juli 1971 in Halle

HUMBOLDT–UNIVERSITÄT ZU BERLIN
Mathematisch–Naturwissenschaftliche Fakultät I
Institut für Physik

Gutachter: Prof. Dr. T. Lohse
              Dr. A. Stahl

Berlin, den 06. Februar 2004

Abstract

One proposed technology for the luminosity calorimeter in the detector of the future TESLA linear collider is a homogeneous crystal calorimeter with longitudinal segmentation and fiber readout.

The luminosity calorimeter located in the forward region of the detector near the beam pipe will be affected by a high radiation dose. Therefore the material of the calorimeter and the readout fibers must have a high radiation hardness.

The material should be as dense as possible, to have a lower Moliére radius.

The scintillation light from a relatively small piece of scintillator has to be coupled into a fiber with a reasonable light yield. The worsening of the time resolution should be reasonable.

Since most crystals create isotropic light through scintillation, in heavy crystals there is light from Čerenkov radiation. The possibility to couple the directed light from Čerenkov radiation into fibers is studied.

The scintillation process in the material must be fast to avoid negative effects on the time resolution of the calorimeter.

Materials must be found that fulfill these requirements.

Several Measurement are presented concerning the absolute light yield, light yield reduction due to the fiber readout and also the time resolution of different materials and readout methods.

In the proposed calorimeter design potential crosstalk between the several segments of the calorimeter and between the segments and the read out fibers could be a problem. Measurements were done to investigate if there is crosstalk between readout fibers crossing a scintillating segment.

Zusammenfassung

Eine der vorgeschlagenen Technologien für des Luminositäts Kalorimeter im Detektor des zukünftigen TESLA Linearbeschleunigers ist ein Kristallkalorimeter mit Tiefensegmentierung und Faserauslese.

Das Luminositätskalorimeter, das sich im Vorwärtsbereich des Detektors nahe des Strahlrohrs befindet, wird einer hohen Strahlungsdosis ausgesetzt sein. Deshalb muss das Material des Kalorimeters eine hohe Strahlenhärte besitzen.

Die Dichte des Materials sollte wegen eines geringeren Moliére Radius so hoch wie möglich sein.

Das Szintillationslicht aus einem relativ kleinen Szintillatorsegment muss mit einer angemessenen Lichausbeute in eine Faser eingekoppelt werden. Dabei sollte die Verschlechterung in der Zeitauflösung nicht zu gross sein.

Während in den meisten Kristallen isotropes Licht durch Szintillation erzeugt wird, tritt in schweren Kristallen Čerenkov-Strahlung auf. Die Möglichkeit, dieses gerichtete Licht in eine Faser einzukoppeln, wird studiert.

Die Dauer des Szintillationsprozesses im Material muss kurz sein, um negative Auswirkungen auf die Zeitauflösung des Kalorimeters zu vermeiden.

In dem vorgeschlagenen Kalorimeterentwurf könnte möglicher Crosstalk zwischen den einzelnen Segmenten des Kalorimeters und den Segmenten und den Auslesefasern ein ernsthaftes Problem sein. Es wurde gemessen, ob es zwischen Auslesefasern und szintillierenden Segmenten zu Crosstalk kommt.

Contents

Chapter 1

Calorimetry

1.1 Principles

Calorimetry in nuclear and particle physics refers to the detection of particles and the measurement of their properties. The calorimeter is a block of matter, where the particles are totally absorbed. The common feature of all existing calorimeters is, that the measurement process through which the particle properties are determined is destructive. The particles lose their energy in several interaction processes (electromagnetic, strong and rarely weak interactions) depending on the energy and the nature of the particles. The only exception to this rule concerns muons. Muons may penetrate the substantial amounts of matter represented by a calorimeter. Up to very high energies the muon loses energy through ionization. The ionization loss is relatively small compared to the energy loss through electromagnetic showers. This fact is important to identify these particles as muons.

1.2 Energy loss of particles in matter

When a charged particle passes matter it looses energy or it is deflected from its incident direction. These effects are the results of inelastic collisions with the atomic electrons of the material or elastic scattering from nuclei. Other processes include emission of Čerenkov radiation, nuclear reactions or bremsstrahlung. Nevertheless, the major part of the energy loss is due to atomic electron collisions. The amount of energy deposited depends on the momentum respectively the energy , the restmass and the charge of the particle and on the properties of the material it passes through.

Electrons and positrons on one hand and particles heavier than the electron (muons, protons, pions, α-particles) on the other hand have to be considered separately. The electronic collision loss by heavy charged particles can be calculated from the Bethe-Bloch formula (equation 1.1) [15].

$$-\frac{dE}{dx} = 2\pi N_A r_e^2 m_e c^2 \rho \frac{Z}{A}\frac{z^2}{\beta^2}\left[\ln\left(\frac{2m_e\gamma^2 v^2 W_{max}}{I^2}\right) - 2\beta^2 - \delta - 2\frac{C_S}{Z}\right] \qquad (1.1)$$

r_e :	classical electron radius	ρ :	density of absorbing material
m_e :	electron mass	z :	charge of incident particle in
N_a :	Avogadro's number		units of e
I:	mean excitation potential	β:	v/c of incident particle
Z:	atomic number of	γ:	$1/\sqrt{1-\beta^2}$
	absorbing material	C:	shell correction
A:	atomic weight of	W_{max}:	maximum energy transfer in
	absorbing material		a single collision

The maximum energy transfer is

$$W_{max} = \frac{2m_e c^2 \eta^2}{1 + 2s\sqrt{1 + \eta^2 + s^2}} \qquad (1.2)$$

with $s = \frac{m_e}{M}$ and $\eta = \beta\gamma$ if $M \gg m_e$, then $W_{max} = 2m_e\eta^2$

Two correction terms are added: the density effect correction

$$\delta = \begin{cases} 0 & , X < X_0 \\ 4.6052X + C_0 + a(X_1 - X)^m & , X_0 < X < X_1 \\ 4.6052X + C_0 & , X > X_1 \end{cases} \qquad (1.3)$$

and the shell correction

$$\begin{aligned} C_s &= \left(0.422377\ \eta^{-2} + 0.0304043\ \eta^{-4} - 0.00038106\ \eta^{-6}\right) \times 10^{-6}\ I^2 \\ &+ \left(3.850190\ \eta^{-2} - 0.1667989\ \eta^{-4} + 0.00157955\ \eta^{-6}\right) \times 10^{-9}\ I^3 \end{aligned} \qquad (1.4)$$

The shell correction parameters C_0, a, m, X_0 and X_1 are material constants.

For electrons and positrons the Bethe-Bloch formula must be modified (equation 1.5). Because of their small mass, electrons and positrons additionally loose energy due to radiation arising in the magnetic field of a nucleus (bremsstrahlung). The Bethe-Bloch formula becomes

$$-\frac{dE}{dx} = 2\pi N_A r_e^2 m_e \rho \frac{Z}{A}\frac{z^2}{\beta^2}\left[\ln\left(\frac{\tau^2(\tau + 2)}{2(I/m_e)^2}\right) + F(\tau) - \delta - 2\frac{C_S}{Z}\right] \qquad (1.5)$$

with

$$F(\tau) = 1 - \beta^2 + \frac{\frac{\tau^2}{8} - (2\tau + 1)\ln 2}{(\tau + 1)^2} \ for \ \mathrm{e}^- \tag{1.6}$$

and

$$F(\tau) = 2\ln 2 - \frac{\beta^2}{12}\left(23 + \frac{14}{(\tau + 2)} + \frac{10}{(\tau + 2)^2} + \frac{4}{(\tau + 2)^3}\right) \ for \ \mathrm{e}^+ \tag{1.7}$$

τ is the kinetic energy of the incident particle in unit of $\mathrm{m}_e c^2$.

By integrating the Bethe-Bloch formula the range of a particle of a given energy can be calculated:

$$R = \int\limits_{E_{kin}}^{0} \frac{dE}{\frac{dE}{dx}} \tag{1.8}$$

This quantity is the penetration depth of particles before they loose all their energy. Figure 1.1 shows the energy loss and the Range of muons in lead. The material constants are listed in table 1.1.
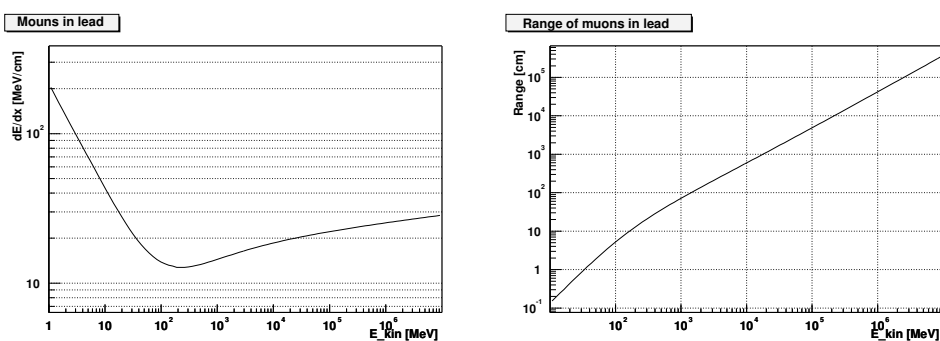
Figure 1.1: *The Energy loss (left) and the range (right) of muons in lead.*

At non-relativistic energies dE/dx is dominated by the overall $1/\beta^2$ factor and decreases to a minimum. Particles at this minimum are called minimum ionizing particles (MIP's). The minimum value is the same for all particles with the same charge. After this minumum dE/dx rises again to relativistic plateau where the $1/\beta^2$ term is almost constant.

1.2.1 Scintillation

Certain materials when struck by a particle emit a small flash of light, the scintillation light. As radiation passes through the scintillator, it excites the atoms and

Parameter	Lead
chem. Formula	Pb
Z	82
A	207.2
ρ [g/cm^3]	11.34
C_0	-6.2
a	0.0936
m	3.16
I [eV]	823
X_1	3.81
X_0	0.3776

Table 1.1: *Material properties of lead [15],[18].*

molecules. A fraction of the energy deposited leads to scintillation. The excited atomic or molecular states are unstable and the excited atom or molecule quickly returns to the ground state and the excitation energy is released in the form of one ore more photons. The light output of a scintillator is directly proportional to the exciting energy respectively to the energy the particle looses in the material. Scintillation detectors are fast instruments in the sense that their response and recovery times are short relative to other types of detectors. The scintillator materials that are in use are organic crystals, organic liquids, plastics, inorganic crystals gases and glasses.

1.2.2 Čerenkov-Radiation

When a charged particle travels faster than the speed of light in a certain medium, it looses energy by emitting Čerenkov radiation (v>c/n, or β=v/c>1/n, with n the refractive index of the medium). The spectrum of Čerenkov radiation exhibits a characteristic $1/\lambda^2$ dependence and, therefore, the visible part of the Čerenkov spectrum is experienced as blue light. The emission of Čerenkov light is only a very minor source contributing to the energy loss of particles. A very important aspect of Čerenkov light is the fact that it is instantaneous. The energy loss comes out naturally from the Bethe-Bloch formula, it is already included in equation 1.1.

Chapter 2

Forward Calorimetry in the TESLA Project

The very forward region of a linear collider detector is a particular challenging area for instrumentation. A large amount of beamstrahlung, several ten TeV per bunch crossing, is scattered into this region, resulting in a radiation dose of about 10 MGy per year. The distribution of the beamstrahlung has to be measured in order to assist in the tuning of the beams at the final focus. On top of that single hard electrons have to be measured, or at least vetoed.

TESLA stands for TeV-Energy Superconducting Linear Accelerator. As proposed in the TESLA Technical Design Report (TDR) [33], TESLA will be a superconducting electron-positron collider of initially 500 GeV total energy, extendable to 800 GeV. The layout of TESLA is shown in figure 2.1.

Figure 2.2 shows the layout of the detector for the TESLA e^+e^- collider as proposed in the TDR [33]. It will be a symmetric detector with a vertex detector around the interaction point surrounded by the tracking system, the electromagnetic and the hadronic calorimeter, the coil and the muon yoke.

2.1   The very forward region and the LCAL

The region of interest for this report is the very forward region in the inner part of the detector directly around the beam pipe (see figure 2.2). Figure 2.3 shows this region in more detail. Two calorimeters, the Low Angle Tagger (LAT) and the Luminosity Calorimeter (LCAL), are mounted inside or in front of a tungsten tube which also acts as shielding of the TESLA detector against radiation created at the beam pipe [22].

A number of different background sources are present in the interaction region. The most severe ones come from beam-beam interactions of the electron and the positron beams. The high charge density of the colliding beams produces strong

electromagnetic fields which bend the trajectories of the particles of the oncoming bunch. This effect increases the collision luminosity, but on the other hand it induces an intense emission of hard beamstrahlung photons ($\sim 6 \cdot 10^{10}$ per bunch crossing with a total energy of about $2.6 \cdot 10^{11}$ GeV). While these photons themselves disappear in the beam pipe, they are a source of background from secondary effects, mainly e^+e^- pairs which stem from conversion of beamstrahlung photons in the high magnetic field densities of the colliding bunches. An area up to the radius of approximately 6 cm is strongly affected by this beamstrahlung.

The Low Angle Tagger (LAT) is expected to give a precision measurement of luminosity, as well as to extend good calorimetric coverage to low angles. The luminosity measurements will be based on detection of Bhabba scattering. The functionality of this process for luminosity determination has been proved in the LEP experiments at CERN. LAT will cover polar angles 27.5 to 83.1 mrad with respect to the beam pipe. The LCAL, as a fast luminosity monitor and as a low angle calorimeter, covers the regime down to very small angles, to 4.6 mrad. Both devices at the same time are a part of the masking system, shielding the detector from backgrounds. In the LAT the radiation background induced by beamstrahlung will be negligible compared to that in the LCAL region.

Thinking of potential technologies for the LCAL it is necessary to have high granularity in order to identify individual hard electrons above the background from beamstrahlung. The transversal granularity should not be larger than a Moliére radius. Otherwise a high amount of beamstrahlung is integrated into the signal from a hard electron and also position measurement becomes less precise. Also a longitudinal segmentation is necessary. The energy deposition of a single 250 GeV electron differs in the longitudinal shape from the energy deposition of hundreds of 0.5 GeV electrons from beamstrahlung.

One proposed technology for the LCAL is a crystal calorimeter with fiber readout. It promises good energy and time resolution. The Moliére radius has to be kept as low as possible. Therfore the material should be as dense as possible.

The standard design of a crystal calorimeter does not provide longitudinal segmentation. A single crystal covering the full depth of a calorimeter is read out from the rear side by photo multiplier tubes or photodiodes. In order to achieve longitudinal segmentation one could cut the crystals into several pieces in depth and read them out with photodiodes. But some photodiodes are then operating in the core of an electromagnetic shower. Many charged particles penetrating the photodiodes and creating signals that are much larger than the signals from the light from the scintillator and thus the calorimeter is transformed into a sampling calorimeter with the crystals as absorbers and the readout diodes as active sensors.

A new idea is to cut the crystals into pieces and attach a readout fiber to every piece. The optical fiber crosses, optical isolated, the crystals to the rear side of the calorimeter (figure 2.1). Then the fibers are routed to areas of lower activity and can be read out by multichannel photo tubes or avalanche photodiodes, but at the

price of lower light yield. The whole structure of such a calorimeter is shown in figure 2.1.

This technology could be used on any crystal calorimeter and is not exclusively connected to the TESLA project.
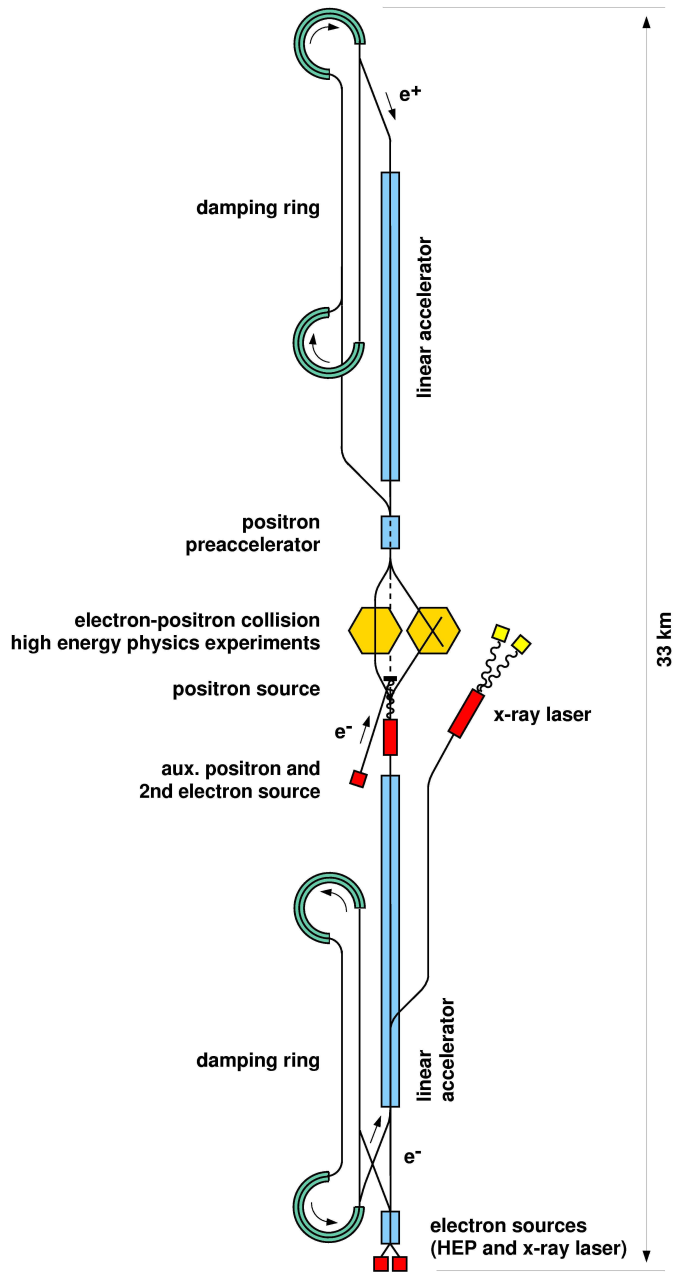
Figure 2.1: *The Layout of TESLA.*
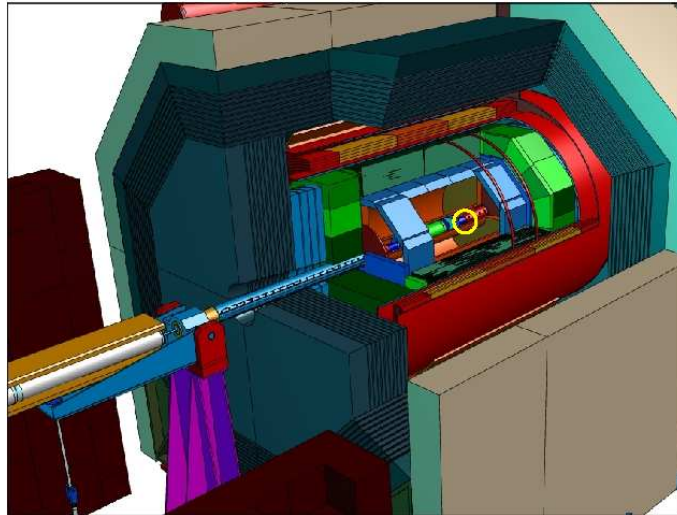
Figure 2.2: *The TESLA-Detector.*
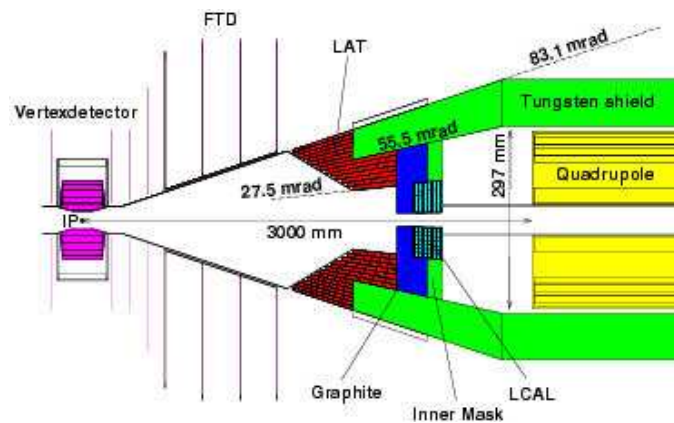
Figure 2.3: *The tungsten shield (mask) near the beam pipe and the two forward calorimeters LAT and LCAL.*
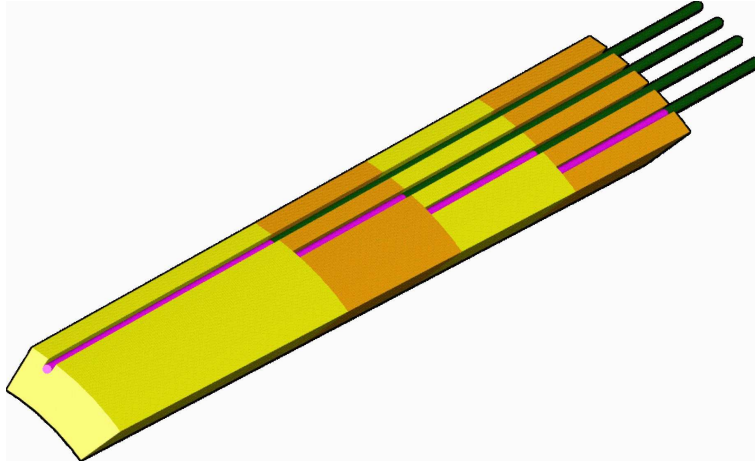
Figure 2.4: *A single scintillator segment with readout fibers.*
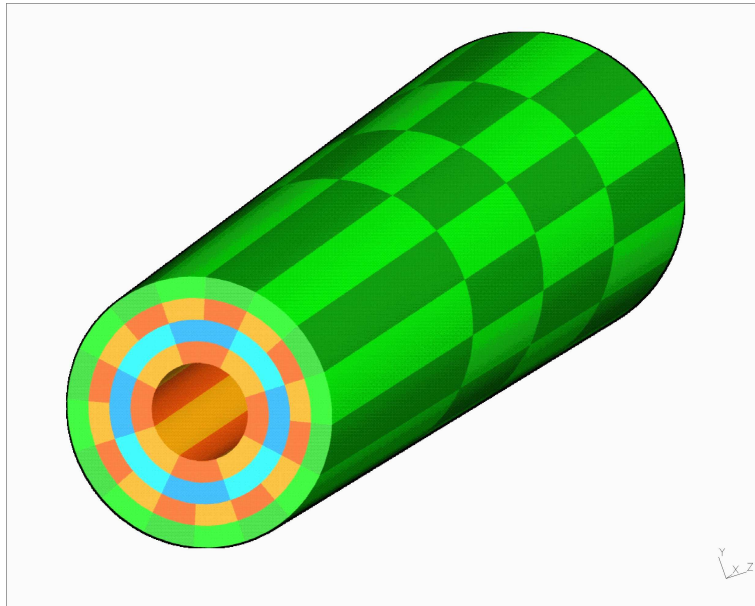
Figure 2.5: *The design of a Calorimeter with longitudinal segmentation.*

Chapter 3

Experimental Setup

The arrangement to measure the light yield and the time resolution of scintillators is a cosmic telescope. Cosmic muons, originating from cosmic ray interaction with the upper atmosphere of the earth, are used as test particles in such an experiment. The flux of the cosmic muons at sea level is about $1/(\text{cm}^2 \text{ min})$. Therfore the event rate with the described setup is relatively low.

The analog signals are digitized with an ADC (Analog to Digital Converter) and a TDC (Time to Digital Converter). These can be read out by a PC for data acquisition with a LabVIEW [12] controlled software. ASCII data files are finally stored, that can easily be processed with analyzing software environments like the C++ based ROOT [23] or the FORTRAN based PAW [19].

The cosmic telescope, placed in a light tight box, consists of two trigger scintillators, vertically aligned with the test sample. A stack of lead is placed between the trigger scintillators to remove low energetic muons (figure 3.1).

3.1 The Photomultiplier Tubes (PMT's)

Two types of photomultipliers were used in this experiment. The two trigger scintillators were read out with HAMAMATSU R7400U metal package photomultiplier tubes [9]. These PMT's are very fast (rise time 0.78 ns) and of compact size (16 mm diameter, 12 mm seated length). Figure 3.3 a) describes the functionality of such kind of a photo tube. For the readout of the several scintillator- and crystal-samples, the linear focused 10-stage dynode PHOTONIS XP1911 photomultiplier tubes were used (figure 3.3 b)) [20]. The XP1911 is not as fast as the R7400U (rise time 2.3 ns), but has a higher quantum efficiency. Furthermore the typical gain, the ratio between primary photoelectrons emitted by the cathode and the measured current at the anode at a certain supply voltage, is higher. The spectral range is almost the same for both types (300-650 nm).

To characterize a photomultiplier, the quantum efficiency is most relevant. The
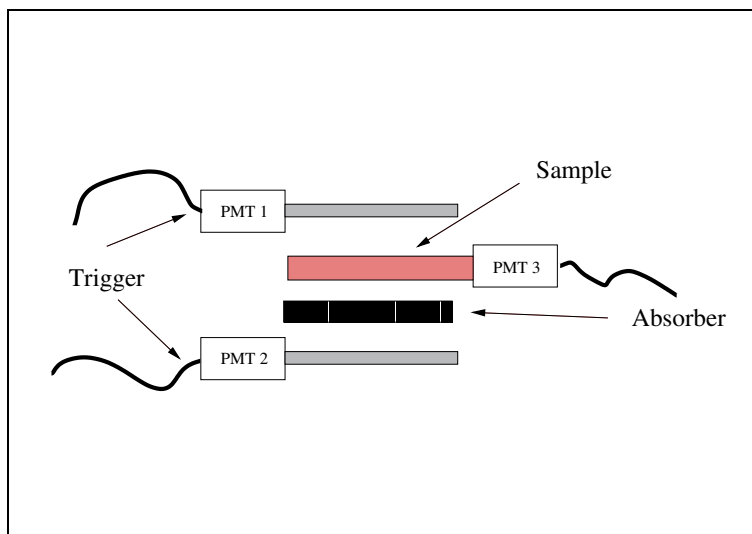
Figure 3.1: *Cosmic Telescope.*

photocathode of the PMT converts incident light into a current of electrons by the photoelectric effect. It is clear that a certain minimum frequency is required, before the photoelectric effect takes place. Above this threshold, the efficiency for photoelectric conversion varies strongly with the frequency of the incident light and the structure of the material of the photocathode. The quantum efficiency $\eta(\lambda)$ expresses the overall spectral response.

$$\eta(\lambda) = \frac{\text{number of released photoelectrons}}{\text{number of incident photons on the cathode with wavelength } \lambda} \qquad (3.1)$$

For PMT's usually the radiant cathode sensitivity $S_r(\lambda)$ is given in units of ampere/watts (figure 3.2). This is the ratio of the photoelectric emission current from the cathode to the incident radiant power. It is related to the quantum efficiency by

$$S_r(\lambda) = \lambda \cdot \eta(\lambda) \cdot \frac{e}{hc} \qquad (3.2)$$

For $S_r(\lambda)$ given in [mA/W] and λ in nanometers the quantum efficency in percent is

$$\eta(\lambda) \rightarrow \text{QE}(\%) \simeq \frac{124}{\lambda(nm)} \cdot S_r(\lambda)[mA/W] \qquad (3.3)$$

Table 3.1 shows the $S_r(\lambda)$ values of the PMT's used. At the wavelength of max. emission of a plastic scintillator (420 nm) the quantum efficency of the XP1911 is 25%, while the R7400U only reaches 20%. Only a quarter of the scintillation light can be detected by the XP1911.

TYPICAL SPECTRAL CHARACTERISTIC
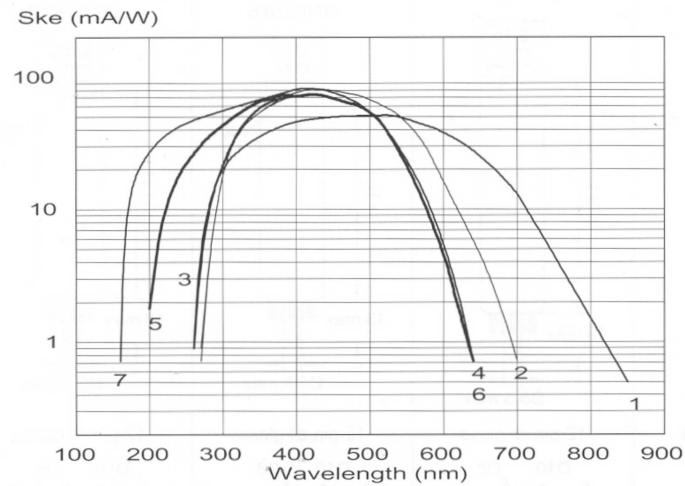
Figure 3.2: *The radiant cathode sensitivity for several photomultiplier tubes. Curve No. 4 corresponds to the XP1911. Figure taken from [20].*

PMT	dynode structure / number	radiant cathode sensitivity $[mA/W]$
XP1911	linear focused / 10	85 at 420 nm [20]
		55 ± 5 at 500 nm (figure 3.2)
R7400U	metal package / 8	62 at 420 nm [9]

Table 3.1: *Dynode structure/number and radiant sensitivity of the PMT's used.*
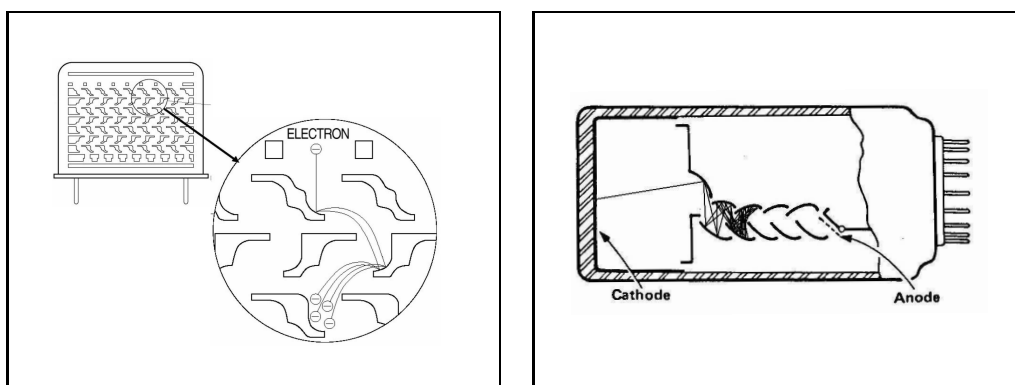
Figure 3.3: *Electron multiplication process in a) a metal package PMT and b) a linear focusing PMT.*

3.2 The Electronics

Besides the ADC [4] and the TDC [13], the electronic devices are standard NIM modules. The ADC itself is a VME-board, read out by a Motorola MVME processor while the TDC is a CAMAC module. A crate controller handles the data transfer between the CAMAC- and the VME-bus.

The 8 channel charge integrating ADC used in this experiment converts the input charge for each channel to a 12-bit word. The full range covers 4096 bins (channels) with a pedestal position, depending on the gate length, at 7 bins per 100 ns gate length. The pedestal position can be shifted to higher bin numbers by using an ADC internal signal source. Both settings were used during the measurements.

The TDC also has 8 independent channels, each of which measures the time from the leading edge of a common start pulse to the leading edge of its individual stop pulse. Each channel disregards any stop pulses received before a start and will accept only one stop for every start. It has three switch-selectable full-scale time ranges, 102 ns, 204 ns and 510 ns, which are digitized to 10 bits (1024 channels) and provide 100 ps, 200 ps and 500 ps resolutions respectively. For the best time resolution, it is operated with time range of 102 ns.

The experiment itself is placed in a light tight box with a feed-through for several signal- and high-voltage-cables. The raw signals from the PMT 1 and 2 (R7400U), connected to the trigger scintillators, are fed into an amplifier with a fixed gain factor of 10 and two identical outputs. The signal from the PMT 3 (XP1911) does not need amplification and is fed into a Fan-In/Fan-Out to divide it as shown in figure 3.4. The signal of each PMT is delayed by cable delays to await the trigger before it is fed into the ADC. The gate length defining the integration time of the ADC is 300 ns. As an example, figure 3.5 shows the signal of PMT 3 in comparison with the signal that arrives at the ADC.

For triggering, the signal of each PMT goes into a discriminator. To assure the synchronization of the signals in the trigger chain, cables of identical length are used between all devices. One output of the discriminator of each PMT is delayed such that it falls in the start- and stop-interval of the TDC.

Another output signal from each discriminator is fed into a logic-unit running in coincidence mode. Here it can be freely chosen, which PMT's have to deliver coincident signals to trigger the readout of the event. This coincidence is used o trigger on cosmic muons. A 1600 ns veto after a coincident signal provides enough time to read and store the whole event.

For calibration purposes the PMT's can be illuminated with an LED running in pulsed mode. The driver unit of the LED provides a synchronous trigger pulse. To monitor the stability of the whole system, a random trigger with variable frequency is available. It consists of two timer modules providing a pulse with adjustable frequency. - It seems to be deceptive to call a device with a fixed frequency random trigger, but since the particles, the measurements are done with (cosmic muons)
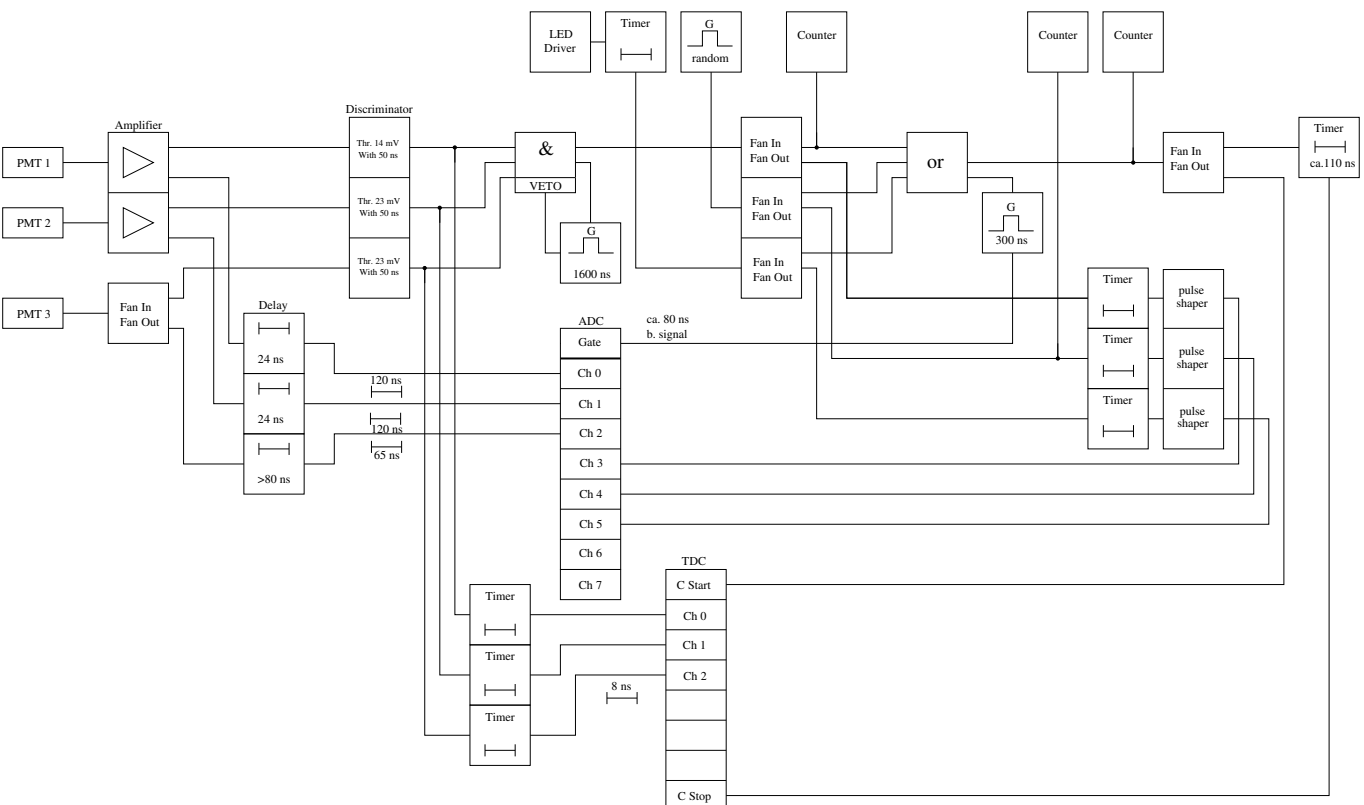
Figure 3.4: *Experimental setup to measure light yields and time resolution with a single phototube.*
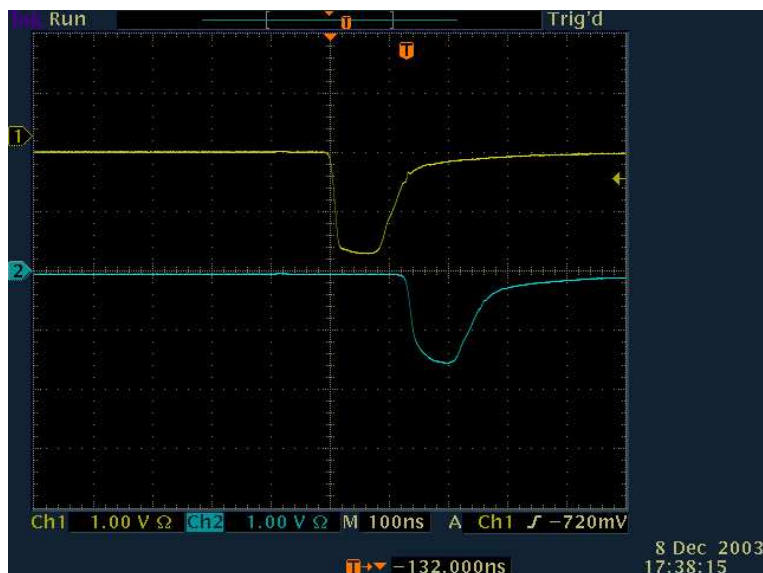
Figure 3.5: *The raw PMT 3 signal (upper curve) and the delayed signal as it arrives at the ADC (lower curve).*

arrive randomly in time, it is a reasonable appellation. - By triggering the readout randomly when no other event has occurred, one has control over the long term behavior of the pedestals (position, width) in each channel.

The three trigger signals are combined in another logic unit operating in or-mode. It is possible to either run the experiment with the coincidence trigger and the random trigger or with the LED trigger and the random trigger or just with one of them. To produce the gate for the ADC the output signal of this unit is adjusted to have a width of 300 ns. It goes directly into the gate input of the ADC. It also provides the start- and, after some delay, the common stop-signal for the TDC. The common stop gives a stop for every TDC channel to terminate the readout, if no signal has arrived in every channel. It was adjusted to arrive 100 ns after the start signal well within the okay time range of the TDC.

The trigger signals from coincidence-, LED- and random-trigger are also fed into ADC channels. This makes offline the information available which of the three signals actually triggered the event (see figure 3.6).

Via a terminal line the measurements can be controlled and monitored by a LabVIEW software module. The ADC- and TDC-readout is done by the MVME processor and the data are saved to disk. The file structure of the output file is shown in figure 3.7. Finally a C++ routine does the trigger selection and creates ROOT files for further analysis.
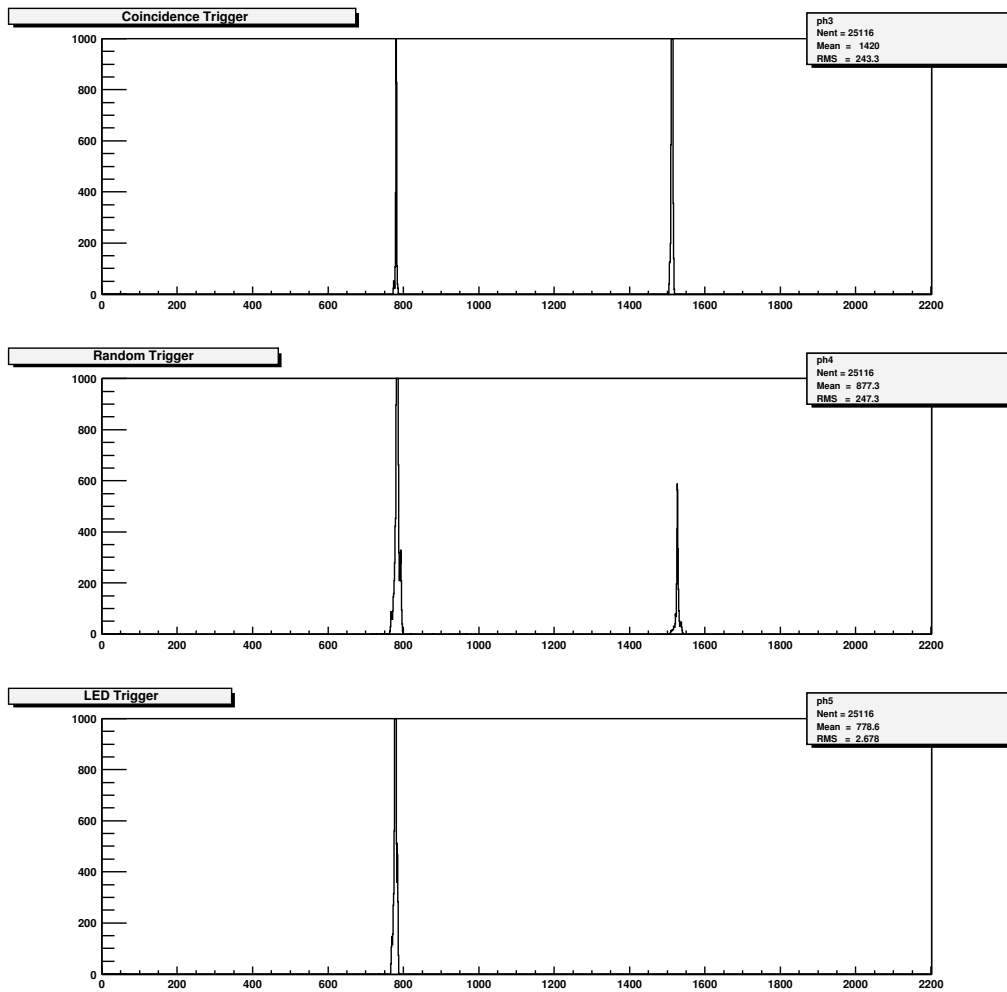
Figure 3.6: *The 3 trigger channels: The left peak in each histogram is the pedestal (trigger = false), the right one the signal peak (trigger = true).*

```
0 LaCoMe(SD) 2.1 2003/09/16 16:24:52
0      Run        35          0          0
0   Comment PMT3 BC 408 sample, direct readout; coinc T1-T2 + rand. Tr.
0 V265[0]        666600        12 0 1 2 3 4 5
0 V262[0]        777700         0        -1        -1        769
0 LC2228[0]          0         8  0.1 0 1 2
1 V265[0]       1323  1365  4061  1513   769   777
1 LC2228[0]      14.7   18.5     36
2 V265[0]        769   766   767   783  1519   780
2 LC2228[0]     100.9  100.2   102.6
3 V265[0]        755   762   765   783  1518   779
3 LC2228[0]     100.9  100.2   102.6
4 V265[0]        773   769   766   783  1518   779
4 LC2228[0]       101  100.2   102.6
5 V265[0]        777   941   754  1512   774   778
5 LC2228[0]      15.4   17.7   102.7
```

Figure 3.7: *The file structure. 2 data lines per event are stored, starting with line number 1. The V265-lines contain 6 ADC-channels (3 PMT-channels, 3 trigger-channels), the LC2228-lines are the 3 TDC-channels.*

Chapter 4

Calibration

4.1 The Principle of Light Yield Measurements

In scintillating material the number of photons emitted is directly proportional to the energy a particle looses in the sample (see section 1.2.1). The number of photons can be obtained from the signal of the PMT attached to the sample. The energy loss can be reliably calculated from the Bethe-Bloch formula (equation 1.1) and the ratio of the two gives the light yield.

Figure 4.1 shows a typical histogram of light output from a scintillator, with the narrow pedestal peak on the left and the wider distribution from ultra-relativistic muons on the right. The distance between the position of the pedestal and the signal peak now gives the information about the number of collected photons at the cathode of the photomultiplier, that is connected to the scintillator sample.
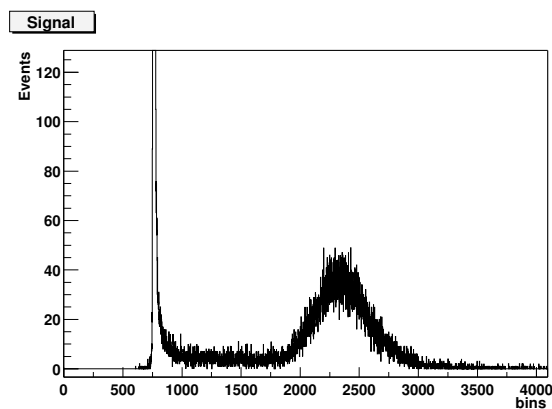
Figure 4.1: *Light output of a scintillator irradiated with ultra-relativistic muons.*

4.2 Calibration of the ADC Scale

As mentioned above, the number of photoelectrons in the photomultiplier is the variable to be measured. One has to perform a calibration of the setup, that gives rise to the signal position expressed in ADC bin numbers and the corresponding number of photoelectrons. This calibration was done with LED's illuminating the photocathode of the phototubes. By varying the LED current, the number of photons emitted by the LED is changed and thus the amount of light "seen" by the photodetectors. In principle there are two calibration methods:

4.2.1 Method 1

When operating the LED with pulses of very low currents, slightly above the threshold where single or just a few photons are emitted by the LED, it is possible to see these single- or double-photoelectron-events in the ADC spectrum separated. Their rate will follow a Poisson distribution in the number of detected photons. Events with n detected photons will create a peak in the spectrum at the position of n photoelectrons with a width increasing like $\sqrt{n}$. To obtain the calibration constant, the following function is fitted to the histogram as seen in figure 4.2.

$$
\begin{aligned}
f_{fit}(p_j) = & \ p_5 \cdot \frac{1}{\sqrt{2\pi}p_6} \cdot e^{-\frac{(x_n - p_2)^2}{2p_6^2}} \\
& + p_4 \cdot \sum_{n=1}^{\infty} \frac{p_0^n}{n!} \cdot e^{-p_0} \cdot \frac{1}{\sqrt{2\pi}\sigma} \cdot e^{-\frac{(x_n - \bar{x})^2}{2\sigma^2}}
\end{aligned}
\tag{4.1}
$$

with

$$
\bar{x} = p_2 + n \cdot p_3 \ , \ \sigma = \sqrt{n} \cdot p_1
\tag{4.2}
$$

The parameters have the following meaning:

- p_0: n = mean number of detected photons

- p_1: noise factor, due to the peak-broadening caused by noise (resolution of the PMT for single photons)

- p_2: pedestal position

- p_3: calibration constant x_0

- p_4: number of events (for normalization purpose)

- p_5: normalization of pedestal peak

- p_6: width of the pedestal peak

The fit algorithm can be reviewed in appendix A.
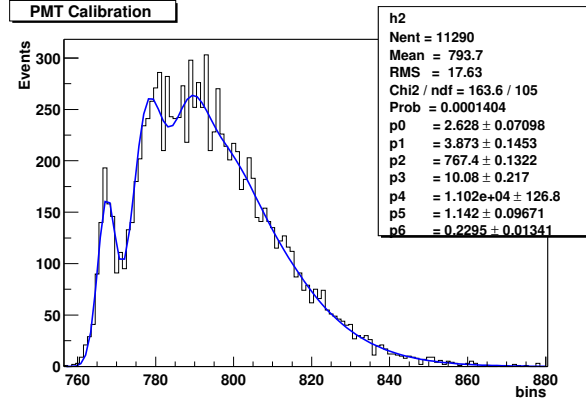
Figure 4.2: *The calibration function (equation 4.1) fitted to the ADC spectrum. The pedestal, the single- and the double-photoelectron-peak are visible. The calibration constant x_0 is the fit parameter p3.*

4.2.2 Method 2

In this method the LED is operated with a higher current and consequently the number of photoelectrons is larger. The PMT output shows a single Gaussian peak (see figure 4.3). All the LED events are contained in the signal peak on the right. The position of the pedestal and signal and the width of the signal peak are used to obtain the calibration constant. The number of photoelectrons is large enough so that Gaussian statistics can be applied to calculate the width of the signal peak. A Gaussian was fitted to the pedestal and the signal and with the distance and the width of the signal peak the calibration constant x_0 can be calculated:

$$n \cdot x_0 = \Delta(x_{signal} - x_{pedestal}) = \bar{x}_2 - \bar{x}_1 \tag{4.3}$$

$$\text{and} \quad \sqrt{n} \cdot x_0 = \sigma_2 \tag{4.4}$$

$$\rightarrow \quad x_0 = \frac{\sigma_2{}^2}{\bar{x}_2 - \bar{x}_1} \tag{4.5}$$

where n is the number of photoelectrons and σ_2 the Gaussian σ of the signal distribution given by the Gauss distribution (equation A.1). With the fit parameters (figure 4.3) equation 4.5 becomes:

$$x_0 = \frac{p_5^2}{p_4 - p_1} \tag{4.6}$$

The fit parameters p_4, p_5 and p_6 are the normalization, the position and the width of the signal peak, respectively and p_1, p_2 and p_3 are the corresponding parameters of the pedestal peak.
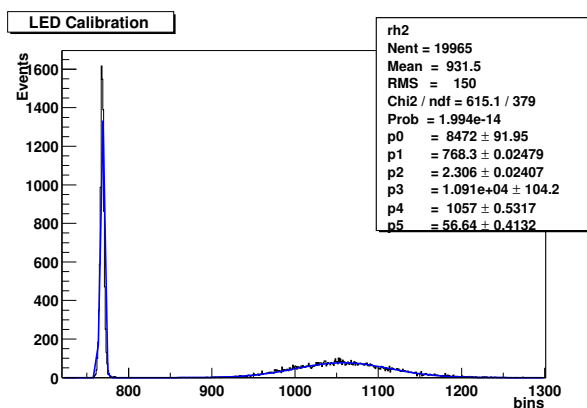
Figure 4.3: *Calibration with method 2.*

Remark: The sections before only describe the principle of the calibration procedure. During the measurements, the system had to be re-calibrated several times, due to changes and adjustments in the readout chain. To have a larger ADC range, the ADC was switched from internal to external signal source for some measurements. Also changes of adjustments of the gate length, discriminator thresholds and the timing of the signals were done. For this reason, the calibration constants are not the same for all the measurements, but were obtained for each measurement as described.

4.2.3   ADC Scale Calibration Results

The first calibration was done with both methods. Figure 4.4 shows the spectra with the fits to obtain x_0 with method 1. All spectra show a slightly increased separation between the pedestal peak and the 1-photoelectron-peak visible at the left flank of the 1-photoelectron-peak. No explanation has been found. It is taken into account in the estimation of the error on the calibration constant.
At higher LED currents several values for the calibration constant were calculated with method 2. The values from both methods are presented in figure 4.5. The upper data points represent method 2. These are the resulting calibration constants in dependence of the number of photoelectrons (n) in the PMT, taken for different intensities of the LED. A straight line was fitted to the data points to determine the average. The lower values inside the frame were obtained with method 1. These do not depend on the number of photoelectrons (x axis) and were plotted with arbitrary values for n.
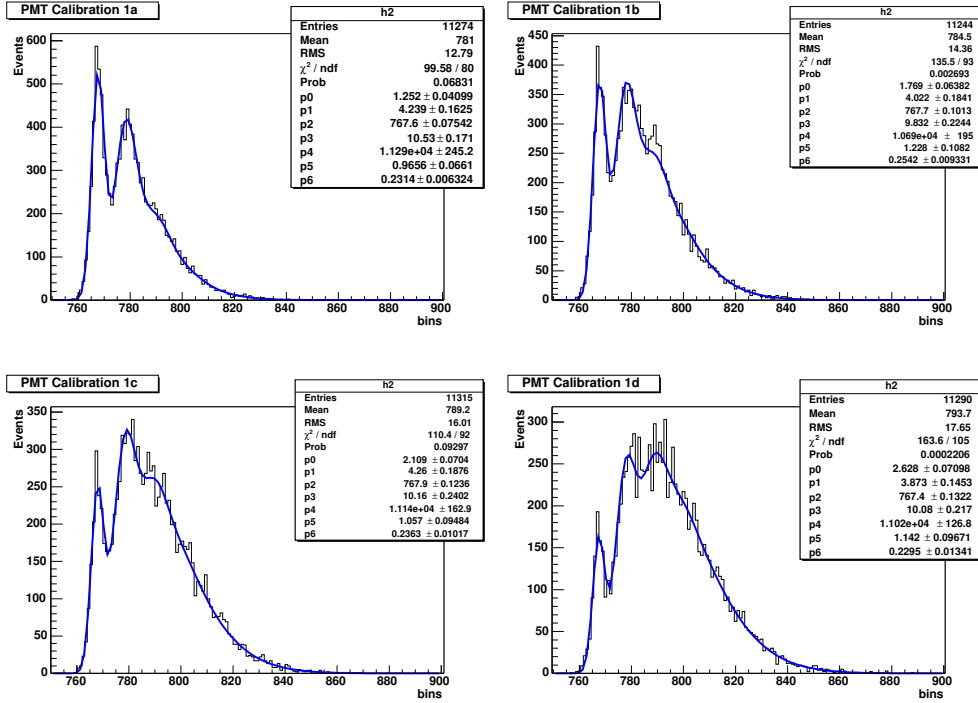
Figure 4.4: *ADC spectra with separated single- and double-photoelectron-peaks. From spectrum a to d the LED current was increased in steps of 1 mA.*

There is a discrepancy between the values of the different calibration methods of 10%. The calibration with method 1 is systematically lower. This is associated with the problem described above. Furthermore it was not possible to perform the method-1-calibration for all three XP1911 PMT's, that were used in the different measurements. Therefore the calibration method 2 was chosen for all ADC scale calibration procedures, but with a systematic uncertainty of the resulting calibration constant of 10%.

Two additional calibration procedures became necessary: Calibration (b) was performed after PMT 4 and PMT 5 ware added to the experimental setup (figure C.1). Besides that, adjustments on the electronics were done and, due to noise problems, signal cables were replaced.

Calibration (c) (figure C.2) was done after the signals of PMT 4 and 5 were fed into the 10x amplifier. Also adjustments of the zero-balance of the Fan-In/Fan-Out device were done and the ADC was switched to internal signal source, so the pedestal position moved to lower bins (see figure B.1).

All resulting calibration curves are presented in appendix C. The final calibration constants for the several PMT's are listed in table 4.1.
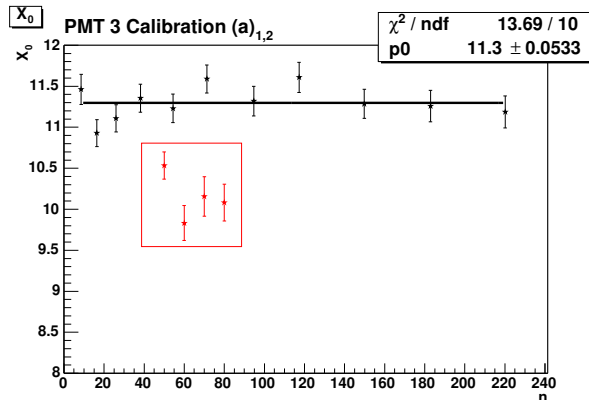
Figure 4.5: *Comparison of the calibration with method 1 and 2 (Calibration (a)). Notice the zero-suppresion of the y-axis.*

Calibration	PMT No.	x_0 [p.e./bin]
(a)	3	11.3 ± 1.1
(b)	3	8.36 ± 0.84
	4	0.976 ± 0.098
	5	5.50 ± 0.55
(c)	3	7.11 ± 0.71
	4	9.07 ± 0.91
	5	59.9 ± 5.9

Table 4.1: ADC calibration constants.

4.3 Calibration of the Time Scale

The TDC measuring the arrival time of the signals covers 102 ns with a time resolution of 100 ps. To calibrate the scale, a rectangular signal was generated and splitted into two. One of these test pulses triggerd the common start while the second one was delayed using identical pieces of LEMO cables with a nominal delay of 5 ns. The delay of the signal was measured by the TDC. Step by step the number of cables was increased. The time delay of each cable chain was measured independently with an oscilloscope (accuracy $\sim$100 ps). Figure 4.6 shows the nominal delay values of each cable chain. With these values a calibration curve for every used TDC channel was taken (figure 4.7).

A linear fit was performed, where the reciprocal of the fit parameter p_1 is the constant to calibrate the TDC scale:

$$time\ [ns] = \left(\frac{1}{p_1}\right) \cdot (TDC\ bin\ number) \tag{4.7}$$

Figure 4.6: *The number of cables per chain and the resulting signal delay as measured with an oscilloscope. The fit parameter p_1 is the actual delay value for a single cable.*

The quality of the linear fits is good enough to consider the TDC scale to be linear. The fact, that the fit parameter p_0 is negative for all TDC channels, indicates that there is a small additional device specific delay. But since no absolute time measurements are done, this effect cancels out. The resulting calibration constants for the TDC channels are listed in table 4.2.

TDC channel	calibration constant $1/p_1$ [ns/bin]
0	1.036 ± 0.007
1	1.043 ± 0.008
2	1.021 ± 0.007

Table 4.2: TDC calibration constants.
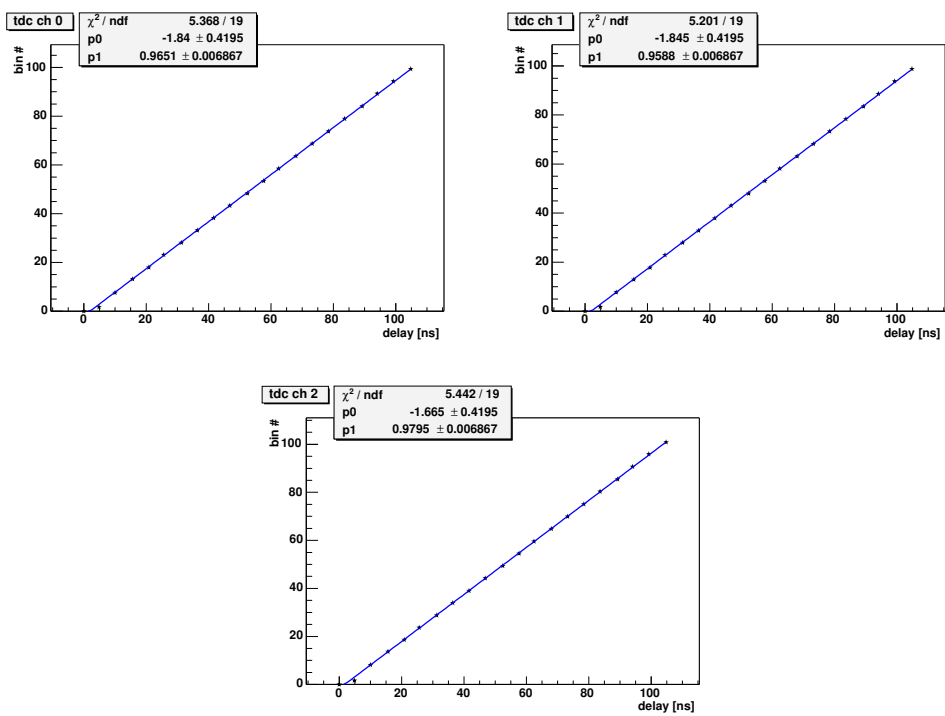
Figure 4.7: *TDC calibration curves.*

Chapter 5

Results of the Measurements

5.1 Light Yield Loss as a Result of the Fiber Readout

In order to study the reduction in light yield due to the fiber readout of scintillator samples, several measurements were performed. First a sample was directly mounted to the PMT by pressing it against the entrance window of the PMT. No optical grease was applied to improve the reproduceability. The absolute light yield of the particular material was determined and compared to the light yield, obtained from measurements, where a scintillating fiber guides the light to the PMT.

The measurements were done with cosmic muons traveling through the sample of interest. From the resulting histogram of each measurement the light yield was calculated. Expressed in the number n of photoelectrons it can be derived using the calibration constant x_0:

$$n = \frac{\bar{x}_{signal} - \bar{x}_{pedestal}}{x_0} \tag{5.1}$$

$\bar{x}_{signal}$ and $\bar{x}_{pedestal}$ are positions of the signal and the pedestal and were obtained from a Gaussian fit to the particular peak in the histogram.

This number of photoelectrons, as discussed before, is the percentage (given by the quantum efficiency of the PMT) of light produced in the material and emitted in the direction, the PMT is mounted.

5.2 The Time Resolution

From the distribution in time the signals arrive at the TDC the time resolution of the samples can be estimated. The width of the signal peak in the TDC spectrum gives the information about the average time interval within which the photons produced in the sample arrive at the PMT. This interval was determined by calculating the full width at half maximum (FWHM) of the signal peak. A Gaussian was fitted to

the signal and the FWHM derived. With the calibration constant for the respective TDC channel (table 4.2) the time interval was derived. The uncertainty of the time resolution is dominated by the accuracy of the TDC. It provides a resolution of 100 ps, therefore the minimal error or the time resolution is 100 ps.

Remark: As one can see in the TDC spectra in the following sections, not all the obtained TDC signals are perfect Gaussian distributions but they are good enough to obtain reasonable values for the width of the signal.

5.3 The Fibers and the Preparation of the Samples

The readout fibers are BICRON BCF-91A [24] wavelength shifting fibers with the emission peak at 494 nm. The optical spectrum of this material can be seen in figure 5.1. The quantum efficiency of the XP1911 PMT decreases for the emission wavelength of BCF-91A of about 500 nm by nearly a factor of two (figure 3.2, table 3.1). The resulting quantum efficiency for the fiber readout is 13 ± 2 %.
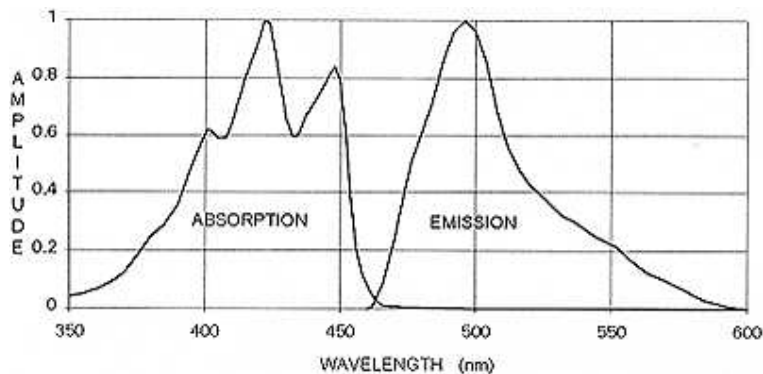
Figure 5.1: *Absorption and emission spectrum of BCF-91A.*

The fibers used have a diameter of 1 mm and were attached to the samples in the following way: Over the whole length a narrow channel was milled into the surface of the sample. With an optical glue the fiber was bonded into the channel.

The surfaces of the samples were well polished and, to increase the reflectivity, the samples were wrapped in TYVEK, a polyethylene paper.

5.4 The Measurements of the different Materials

5.4.1 BC-408 - Polyvinyltoluene $[CH_3C_6H_4CHCH_2]_n$

BICRON BC-408 [24] is a polyvinyltoluene based plastic scintillator with a wavelength of maximum emission of 425 nm. 425 nm is in the range of highest radiant

sensitivity of the XP1911 photo multipliers (figure 3.2). Table 5.1 shows the material composition of the scintillator material.

Element	Z	fraction by weight
H	1	0.5247
C	6	0.4753

Table 5.1: *Material composition data of BC-408.*

Two samples of BC-408 were used for the light yield measurements. Both have the dimensions of 6 x 6 x 30 mm^3 (see figure 5.2). To one of the samples a scintillating fiber (length 210 mm) was attached as described above. While the sample with the fiber is completely wrapped in TYVEK (figure B.3), one face of the plain sample was left open to attach it directly to the photo multiplier. The scintillator samples are sketched in figure 5.2.
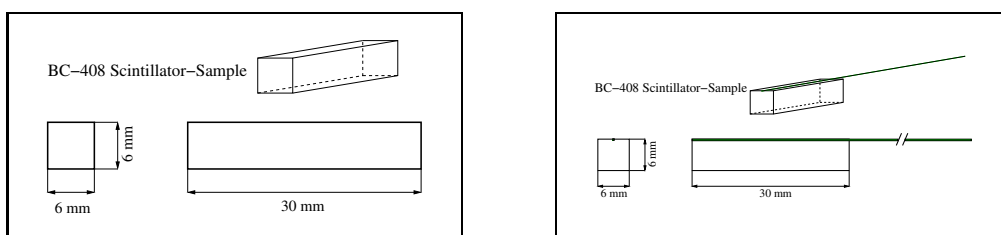
Figure 5.2: *BC-408 Samples without (left) and with readout-fibers (right).*

The parameters to calculate the energy loss of cosmic muons in the material with the Bethe-Bloch formula (equation 1.1) are listed in table 5.2. Figure 5.3 shows the result of this calculation. The vertical line indicates the energy cutoff due to the Pb-absorber with a thickness of 2 cm. Muons with an energy lower than 50 MeV cannot pass the absorber. The muons from cosmic ray interaction have an energy above the value for minimum inonization. When they reach the surface of the earth their energy is still high enough to be in the relativistic plateau of the Bethe-Bloch curve. The energy loss of the ultra-relativistic muons (URM) with an energy of 2 $\sim$ 4 GeV in a BC-408 sample of thickness of 6 mm is

$$E = 1.40 \pm 0.04 \ MeV \qquad (5.2)$$

5.4.1.1 BC-408 Direct Readout

Figure 5.4 shows the setup for the measurements of the light yield for direct readout. The plain BC-408 sample is arranged between the trigger scintillators and the PMT 3 is attached to the open side of the sample.

Parameter	BC-408
$Z_{(eff.)}$	64
$A_{(eff.)}$	118.18
ρ [g/cm^3]	1.032
C_0	-3.201
a	0.3495
m	2.749
I [eV]	64.7
X_1	2.2
X_0	0.1467

Table 5.2: *Material properties of BC-408 [28].*
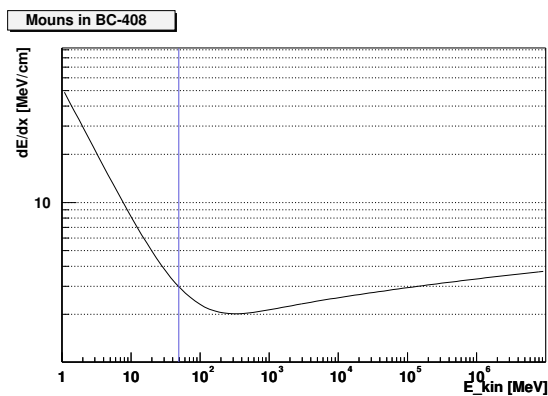
Figure 5.3: *The energy loss of muons in BC-408.*

Figure 5.5 and 5.6 show the histograms and distance fits of two direct-readout measurements. The results are listed in table 5.3. These values are in good agree-

No.	p.e. / URM	p.e. / MeV
1	386 ± 41	277 ± 36
2	401 ± 42	288 ± 38

Table 5.3: *BC-408 light yields - direct readout.*

ment with each other and the average is

$$n_{p.e.}(\text{BC-408/dr}) = 390 \pm 50 \ p.e. \ per \ URM \tag{5.3}$$

The light yield in units of deposited energy in the sample is

$$n_{p.e.}(\text{BC-408/dr}) = 280 \pm 40 \ p.e. \ per \ MeV \tag{5.4}$$
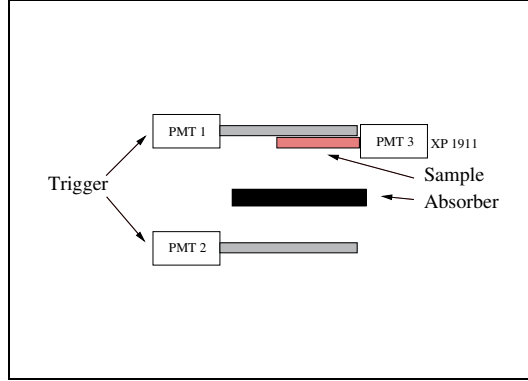
Figure 5.4: *Illustration of a cosmic telescope with the arrangement of the sample of interest between the trigger scintillators. Note: The particular samples used have different dimensions.*

With the quantum efficiency of the PMT of 25 ± 1 % at 425 nm (max. emission wavelength of BC-408) the absolute light yield can be derived:

$$n_{ph}(\text{BC-408/dr}) = 1560 \pm 260 \; photons \; per \; URM \qquad (5.5)$$

$$n_{ph}(\text{BC-408/dr}) = 1120 \pm 21 \; photons \; per \; MeV \qquad (5.6)$$

5.4.1.2 BC-408 Fiber Readout

In figure 5.7 the experimental setup for the fiber readout measurements is sketched. Four measurements with cosmic muons were done. Figure 5.8 and figure 5.9 show the resulting histograms from two measurements. The values for all measurements are given in table 5.4.

No.	p.e. / URM	p.e. / MeV
3	29.6 ± 2.9	21 ± 3
4	27.8 ± 2.9	20 ± 3
5	25.4 ± 2.8	18 ± 3
6	24.5 ± 3.4	18 ± 3
av.	27 ± 3	19 ± 3

Table 5.4: *Light yields - fiber readout. The values for the light yield are the number of photoelectrons released from the cathode of the PMT.*

The values for the obtained light yield vary within a range of 15%. This is taken as an estimate of the systematic uncertainty of the fiber readout method. Most likely this is due to inhomogeneities across the photocathode of the PMT.
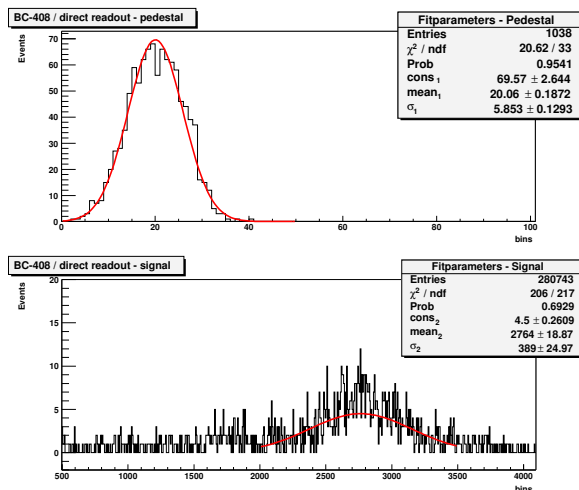
Figure 5.5: *BC-408 - direct readout, measurement No. 1. The calibration constant is $x_0 = 7.1 \pm 0.7$ p.e./bin).*

The resulting number of photoelectrons for the fiber readout method is

$$n_{p.e.}(\text{BC-408/fr}) = 27 \pm 4 \ p.e. \ per \ URM \tag{5.7}$$

and in unit of the energy

$$n_{p.e.}(\text{BC-408/fr}) = 19 \pm 3 \ p.e. \ per \ MeV \tag{5.8}$$

With a quantum efficiency of the photo multiplier of 13 ± 2 % at 500 nm the absolute number of photons guided by the scintillating fiber to the photocathode is

$$n_{ph}(\text{BC-408/fr}) = 150 \pm 40 \ photons \ per \ MeV \tag{5.9}$$

5.4.1.3 The Time Resolution of BC-408

In figure 5.10 and figure 5.11 the distribution in time of signals from both readout methods of the scintillator samples are presented.

The resulting widths and the corresponding time intervals Δt in [ns] are listed in table 5.5. Δt was calculated using the calibration constant for TDC channel 2 of 1.021 ± 0.007 ns/bin.

5.4.1.4 BC-408 - Results

For BC-408 the light yield obtained with the fiber readout is reduced to 14 ± 6 % compared to the direct readout. The time resolution of the fiber readout is by a factor of 2 worse.
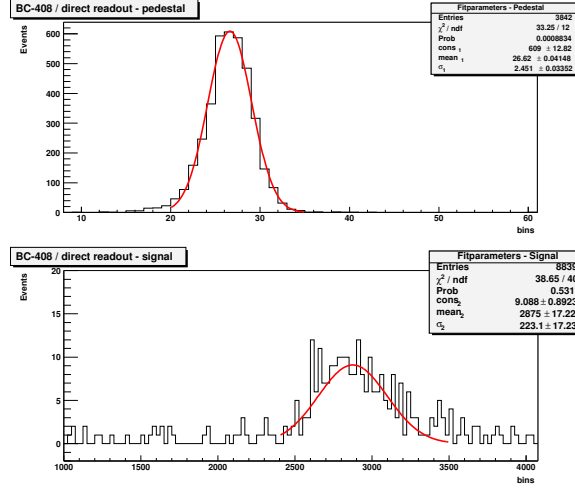
Figure 5.6: *BC-408 - direct readout, measurement No. 2, ($x_0 = 7.1 \pm 0.7$ p.e./bin).*

	No.	FWHM	Δt [ns]
direct readout	1	1.51 ± 0.05	1.6 ± 0.1
	2	1.32 ± 0.07	1.4 ± 0.1
fiber readout	4	3.0 ± 0.1	3.1 ± 0.1
	5	2.42 ± 0.06	2.5 ± 0.1

Table 5.5: *BC-408 Time resolution.*

5.4.2 Lead Glass

Lead glass is a Čerenkov radiator. The lead glass sample has the dimensions 40 x 10 x 10 mm^3 (figure B.3). The material is SF57 made by SCHOTT Glaswerke [26], [27]. SF57 is an optical glass with the density $\rho = 5.51$ g/cm^3 and a fraction of lead of 75%. The typical material composition of lead glass and the material fractions can be seen in table 5.6. For this particular material no correction parameters for the Bethe-Bloch formula were found, therefore the obtained values for the light yield are given in photons/URM. The quantum efficiency of the PMT for Čenrenkov light (blue light, $\lambda \sim 460 \sim 490nm$) the quantum efficiency is 15 ± 2 %.

One lead glass sample was used in the measurement. It has a readout fiber attached to it in the way as described in section 5.3. The sample is completely wrapped in TYVEK. Both measurement methods, the direct readout method and the fiber readout method were performed with the same sample.
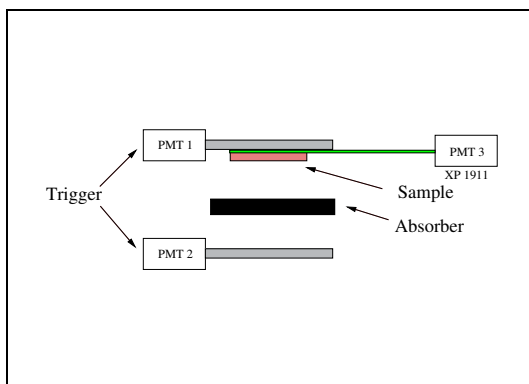
Figure 5.7: *Experimental setup to measure the light yield of a sample with fiber readout.*

Element	Z	fraction in [%]
O	8	16
Si	14	8
Ti	22	0.8
As	33	0.0.2
Pb	82	0.75

Table 5.6: *Material composition data of lead glass.*

5.4.2.1 Lead Glass Direct Readout

For the direct readout method the face opposite to the readout fiber coming out was opened. The sample was turned around and mounted to the cathode window of the PMT. Figure 5.12 shows the resulting histogram of the direct readout measurement. The ADC calibration constant for this measurement is

$$x_0 = 7.1 \pm 0.7 \ p.e./bin \tag{5.10}$$

The resulting number of photoelectrons for the direct readout is

$$n_{p.e.}(\text{LG/dr}) = 18.2 \pm 2.2 \ p.e. \ per \ URM \tag{5.11}$$

and with the quantum efficiency of the PMT of 15 ± 2 % the absolute light yield is

$$n_{ph}(\text{LG/dr}) = 120 \pm 30 \ photons \ per \ URM \tag{5.12}$$

5.4.2.2 Lead Glass Fiber Readout

From the fiber readout of the lead glass sample, the histogram shown in figure 5.13 was obtained.
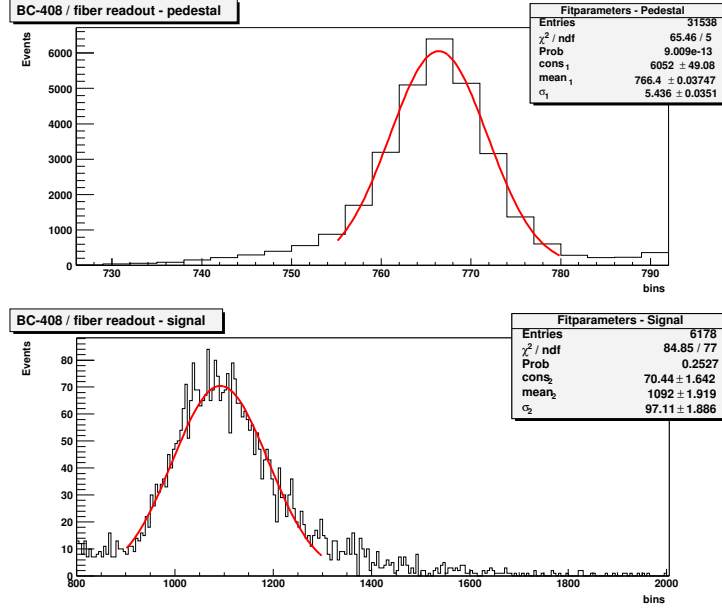
Figure 5.8: *BC-408 fiber readout, measurement No. 3 (calibration constant $x_0 = 11 \pm 1$ p.e./bin).*

After an appropriate re binning of the histogram the fits were performed and the resulting number of photoelectrons of the fiber readout was calculated:

$$n_{p.e.}(\text{LG/fr}) = 2.4 \pm 0.5 \ p.e. \ per \ URM \tag{5.13}$$

with the quantum efficiency for the fiber readout the number of photons is

$$n_{ph}(\text{LG/fr}) = 19 \pm 7 \ photons \ per \ URM \tag{5.14}$$

5.4.2.3 The Time Resolution of Lead Glass

The TDC spectra of both readout methods are presented in figure 5.14.

	No.	FWHM	Δt [ns]
direct readout	7	1.97 ± 0.07	2.0 ± 0.1
fiber readout	8	4.4 ± 0.6	4.5 ± 0.6

Table 5.7: *Lead Glass Time resolution.*

Table 5.7 shows the values for the time resolution of lead glass for both methods.
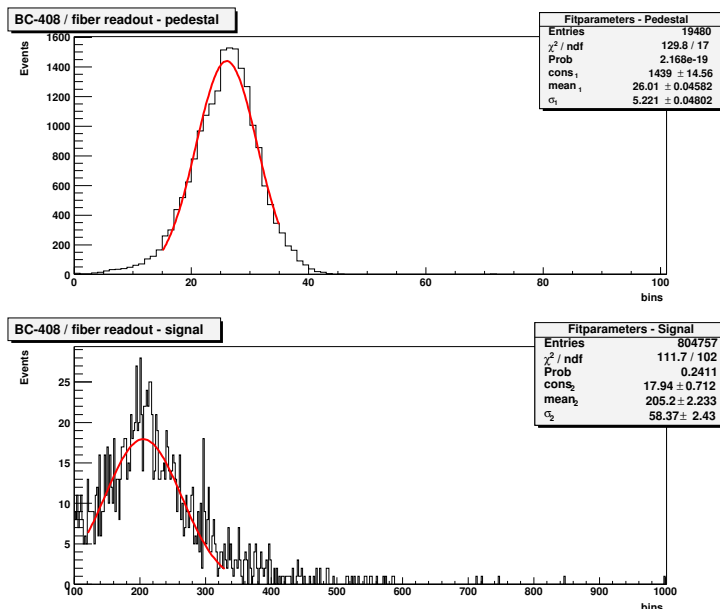
Figure 5.9: *BC-408 fiber readout, measurement No. 5 (calibration constant $x_0 = 7.1 \pm 0.7$ p.e./bin).*

5.4.2.4 Lead Glass results

The light yield of the fiber readout compared to the direct readout of lead glass is reduced to 16 ± 9 %. This is within the uncertainties the same as it is for BC-408. The time resolution is worse than the time resolution of the BC-408 sample, but the broadening due to fiber readout of the time interval within which the signals arrive at the TDC is of the same order.

5.4.3 Double Natrium-Bismuth Tungstate NaBi(WO$_4$)$_2$

Double Natrium-Bismuth Tungstate is a transparent material with a yellow glimmer. The sample used has the dimensions of 22.2 x 22.2 x 17.5 mm^3 and was produced at the Georgian State University, Tbilisi. The material has a high density of $\rho = 7.7$ g/cm^3 and it resists radiation up to 10^8 rad (= 1MGy). The wavelength of max. emission is 520 nm, thus the quantum efficiency of the PMT is 11 ± 2 % (see also figure B.4). The sample is wrapped in TYVEK with a window left open at one face to attach it to the PMT. The measurement was done analogous to the measurements with the other materials. It was placed between the trigger scintillators like sketched in figure 5.4.
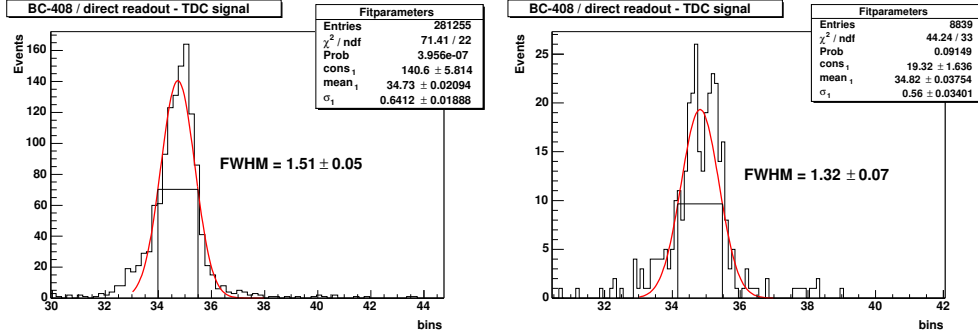
Figure 5.10: *TDC signals from the BC-408 sample. Direct readout measurement No.1 (left) and measurement No.2 (right).*
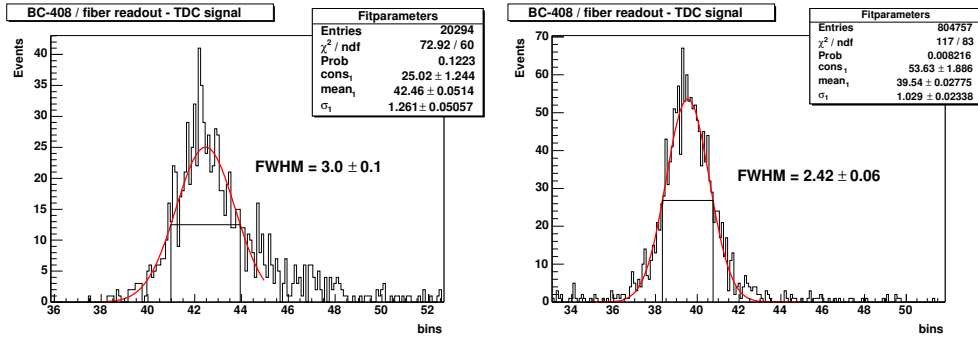
Figure 5.11: *TDC signals from the BC-408 sample. Fiber readout measurement No. 4 (left) and measurement No. 5 (right).*

5.4.3.1 Light Yield

The histogram for the light yield measurement of NaBi(WO$_4$)$_2$ is shown in figure 5.15.

With the results of the fit and the calibration constant x$_0$ = 7.1 ± 0.7 p.e./bin the number of photoelectrons is

$$n_{p.e.}(\text{NaBi(WO}_4)_2/\text{dr}) = 11.7 \ \pm \ 1.5 \ p.e. \ per \ URM \tag{5.15}$$

and the absolute light yield with 11 ± 2 % quantum efficiency is

$$n_{ph}(\text{NaBi(WO}_4)_2/\text{dr}) = 94 \ \pm \ 30 \ photons \ per \ URM \tag{5.16}$$

5.4.3.2 The Time Resolution of NaBi(WO$_4$)$_2$

Figure 5.16 shows the distribution in time of the collected events in the NaBi(WO$_4$)$_2$ sample.

Lead glass / direct readout - pedestal		Fitparameters - Pedestal	
		Entries	6703
		χ^2 / ndf	30.34 / 12
		Prob	0.00248
		$cons_1$	861 ± 14.23
		$mean_1$	24 ± 0.03874
		σ_1	2.932 ± 0.034

Lead glass / direct readout - signal		Fitparameters - Signal	
		Entries	2074
		χ^2 / ndf	155.8 / 154
		Prob	0.4452
		$cons_2$	4.615 ± 0.3164
		$mean_2$	156.8 ± 2.669
		σ_2	46.23 ± 3.689
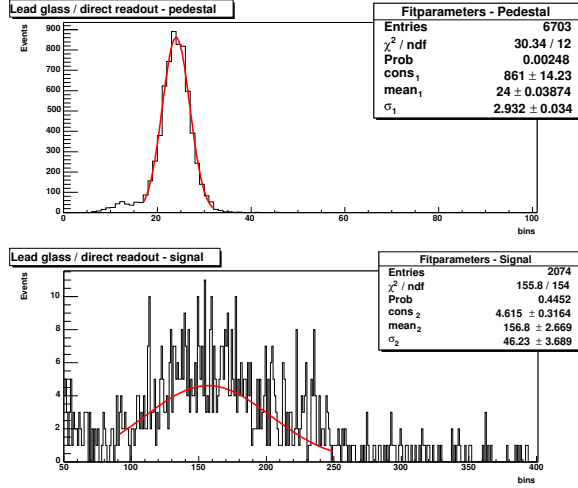
Figure 5.12: *Lead glass - direct readout.*

With the calibration constant of the TDC channel 2 the resulting time resolution of $NaBi(WO_4)_2$ is

$$FWHM = 1.48 \pm 0.05 \ \rightarrow \ \Delta t = 1.5 \pm 0.1 \ ns \tag{5.17}$$

5.4.3.3 $NaBi(WO_4)_2$ Results

$NaBi(WO_4)_2$ has an absolute light yield of 94 ± 30 photons per URM. This is comparable to the obtained light yield from lead glass. The time resolution of $NaBi(WO_4)_2$ is as good as the time resolution of a fast scintillator like the BC-408.

5.5 Crosstalk

Figure 5.17 shows a sketch of the sample, the crosstalk measurements were performed with. This sample consists of three identical samples of BC-408, every sample wrapped with TYVEK. Readout fibers are attached to every single sample and routed to one side. The fibers, where they cross other samples, are optical isolated with black paint (see also figure B.4).

For this measurement 2 additional XP1911 PMT were added to the experiment. The signals of these 2 PMT's are amplified (see figure B.1).

The setup with the 3x-sample in between the trigger scintillators is sketched in figure 5.18. The readout of all tree sample is triggered by an event of sample c. The histograms of all three PMT's shown in figure 5.19 were obtained. The sample in between the trigger scintillator gives a clear signal. Events, that made no signal in sample c are cut out. There are so signals in the other readout fibers. Two events,
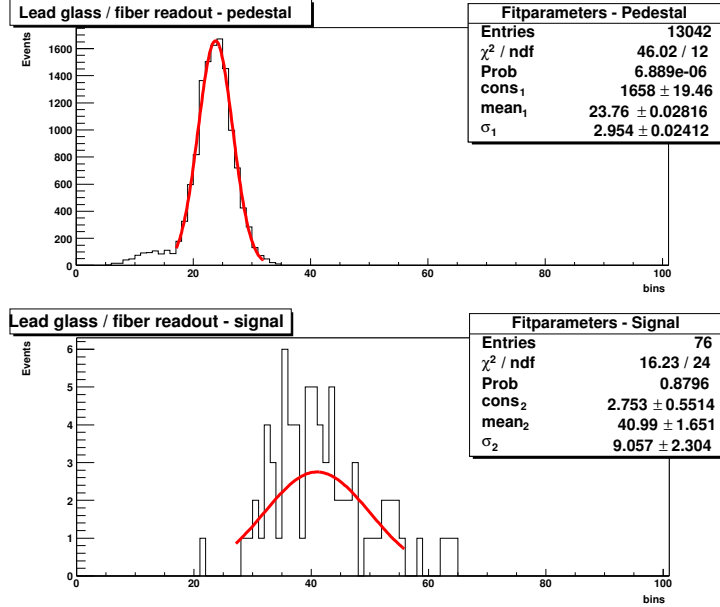
Figure 5.13: *Lead glass - fiber readout.*

that are above the threshold were the the PMT's can see a single photoelectron (this threshold is similar to the calibration constant of that PMT), are marked in the histograms. These single events are most likely signals due to noise in the electronic readout devices. The measurement could be reproduces several times. No crosstalk has been seen the other measurements. This is a very promising result of the measurement. If there is crosstalk between the fibers and the segments they cross it is on the level of the noise of the photo multipliers and the electronics and below the threshould of the PMT for detecting single photoelectron events.

To compare the light yield to the light yield of the single BC-408 sample the signal of sample c was fitted (figure 5.20. The obtained value for the light yield is with

$$n_{p.e.}(\text{3x-sample / fr}) = 25 \ \pm \ 3 \ p.e. \ per \ URM \tag{5.18}$$

exactly the same like for the single sample with fiber readout.
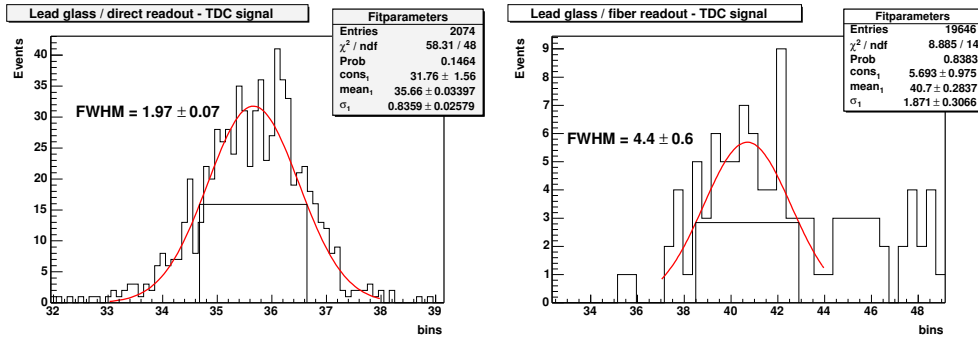
Figure 5.14: *TDC signals from Lead Glass. Direct readout measurement No.7 (left) and fiber readout measurement No.8 (right).*
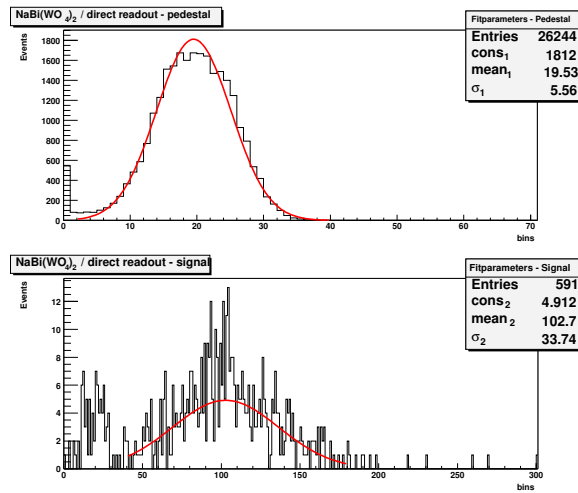
Figure 5.15: *NaBi(WO₄)₂.*
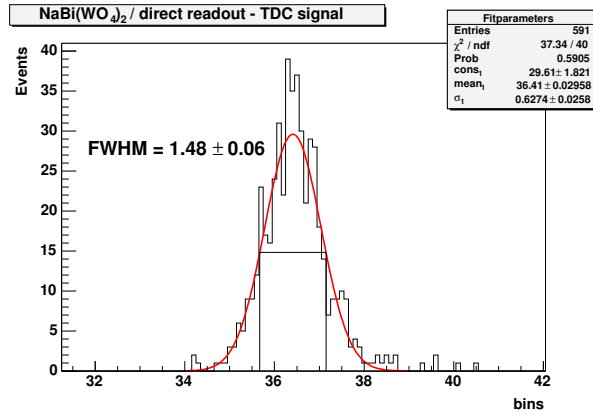
Figure 5.16: *The Time Resolution of NaBi(WO$_4$)$_2$.*
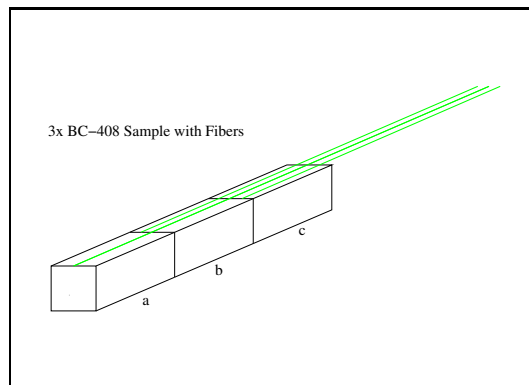
Figure 5.17: *BC-408 3x-Sample with fibers.*
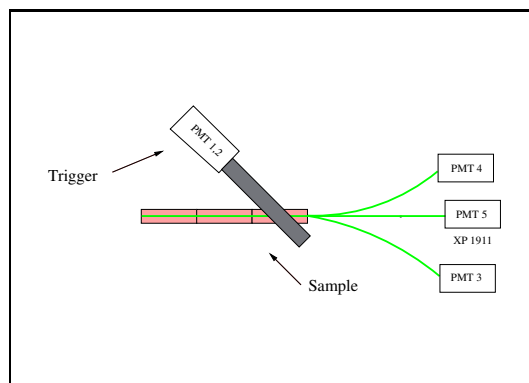
Figure 5.18: *Cosmic telescope for crosstalk measurements. View from above.*
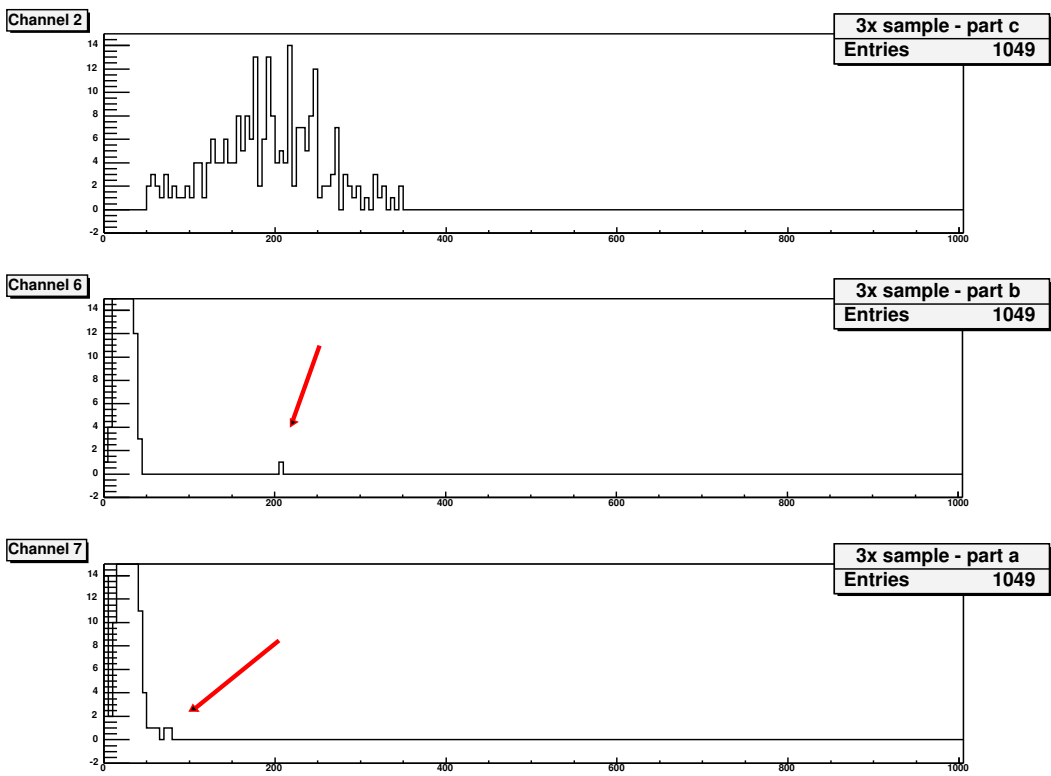
Figure 5.19: *Crosstalk measurement. The calibration constants are* $x_0(c) = 7.1 \pm 0.7$ *p.e./bin,* $x_0(b) = 9.07 \pm 0.91$ *p.e./bin and* $x_0(a) = 59.9 \pm 5.9$ *p.e./bin.*
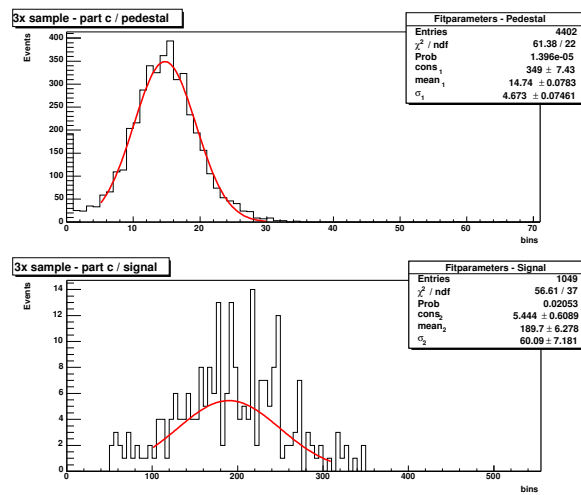
Figure 5.20: *3x-sample: part c light yield fit.*

5.6 Summary and Conclusions

Several measurements have been accomplished to investigate the feasibility of a crystal calorimeter with longitudinal segmentation. The light yield and the time resolution of different materials were determined and the reduction in light yield due to the readout with scintillating fibers was determined. It was studied, wether potential crosstalk between the segments and the particular readout fibers of such a calorimeter will be a serious problem.

The results of the light yield measurements are promising. The light yield obtained with the fiber readout method compared to a direct readout is reduced to 14 ± 6 % for the BC-408 scintillator sample and to 16 ± 9 % for the Čerenkov radiator lead glass.

In a complete calorimeter structure, it should be possible to guide a reasonable amount of light to photo detectors placed outside of the structure. Improvements in the matching of the fibers to the samples, in the surface treatment of the samples or in a better matching of the photo detectors to the readout fibers used (radiant sensitivity and max. emission wavelength) should increase the light yield.

The properties of a novel scintillator, Double Natrium-Bismuth Tungstate $NaBi(WO_4)_2$, were studied. The absolute light yield of the sample used in this experiment is 94 ± 30 photons per ultra-relativistic muon. This heavy material (density $\rho = 7.7$ g/cm^3, Moliére radius $r_m = 2.3$ cm) is very radiation hard, it resists radiation up to 10^8 rad. It is a candidate material for calorimeter applications in regions with high radiation exposure of future detectors, but not for the TESLA-Detector. The light yield of $NaBi(WO_4)_2$ is comparable to the light yield of lead glass (ly $= 120 \pm 30$ photons per ultra-relativistic muon) and with a time resolution of $\Delta t = 1.5 \pm 0.1$ ns it is as fast as a plastic scintillator.

No evidence of crosstalk between the scintillators or a scintillator and a crossing readout fiber was found. If there is any crosstalk, it is below the sensitivity reached here.

The basic principle of longitudinal segmentation by separating the scintillator longitudinally and extracting the light through fibers has been demonstrated successfully on different materials. The next step should now be the test of a full calorimeter segment.

5.7 Zusammenfassung und Schlussfolgerungen

Um die Machbarkeit eines Kalorimeters mit Tiefensegmentierung zu untersuchen wurden verschiedene Messungen durchgeführt. Die Lichtausbeute und die Zeitauflösung verschiedener Materialien wurde bestimmt und die Reduzierung der Lichtausbeute durch die Auslese mittels szintillierender Fasern bestimmt. Es wurde untersucht, ob ein potentieller Crosstalk zwischen den Segmenten und den Fasern eines solchen Kalorimeters ein ernsthaftes Problem werden könnte.

Die Resultate der Lichtausbeutemessungen sind vielversprechend. Die gewonnene Lichtausbeute der Faserauslesemethode beträgt im Vergleich zu einer direkten Auslese 14 ± 6 % für den BC-408 Szintillator und 16 ± 9 % für Bleiglas, das Čerenkovlicht aussendet.

In einem kompletten Kalorimeter sollte es möglich sein, eine angemessene Lichtmenge zu den Fotodetektoren ausserhalb des Kalorimeters zu leiten. Verbesserungen bei der Verbindung der Fasern mit den Szintillatoren, bei der Oberflächenbehandlung der Stücke und eine verbesserte Abstimmung der Fotodetektoren und der Fasern (Strahlungssensitivität und Wellenlänge der maximalen Emission) sollten die Lichtausbeute verbessern.

Weiterhin wurden die Eigenschaften eines neuartigen Szintillators untersucht: Natrium-Wismut-Wolframat $NaBi(WO_4)_2$. Die absolute Lichtausbeute der Probe, die untersucht wurde, ist 94 ± 30 Photonen pro hochrelativistischem Müon. Dieses schwere Material (Dichte $\rho = 7.7$ g/cm^3, Moliére Radius $r_m = 2.3$ cm) ist sehr strahlungshart, es kann Strahlung bis zu 10^8 rad aushalten. Dieses Material ist ein Kanditat für Kalorimeteranwendungen in Bereichen, die hoher Strahlung ausgesetzt sind, jedoch nicht für den TESLA-Detektor. Die Lichtausbeute von $NaBi(WO_4)_2$ ist vergleichbar mit der von Bleiglas (ly $= 120 \pm 30$ Photonen pro hochrelativistisches Müon) und mit einer Zeitauflösung von $\Delta t = 1.5 \pm 0.1$ ns ist es so schnell wie ein Plastik-Szintillator.

Es wurden keine Hinweise für Crosstalk zwischen den Szintillatoren oder den Szintillatoren und den darüberfuehrenden Fasern gefunden. Wenn Crosstalk auftritt, so ist dieser unterhalb der Empfindlichkeit, die hier erreicht wurde.

Das Grundprinzip einer Tiefensegmentierung eines Szintillators, dessen Segmente mittels Szintillierender Fasern ausgelesen werden, wurde erfolgreich an verschiedenen Materialien demonstriert. Der nächste Schritt sollte der Test eines kompletten Kalorimetersegments sein.

Appendix A

Functions - Algorithms

The Gauss equation used fot the Gaussian fits:

$$G(x) = \frac{1}{\sqrt{2\pi}\sigma} \cdot e^{-\frac{(x-\bar{x})^2}{2\sigma^2}} \tag{A.1}$$

The poisson equation:

$$P(i) = \frac{\mu^i}{i!} \cdot e^{-\mu} \tag{A.2}$$

The fit algorithm for the ADC calibration (method 1):

```
Double_t FitFunc(Double_t *x, Double_t *par)
{
  Double_t fu =0;
  int n;
    Double_t p,mean,sigma;
    int nmax = 10;
    Double_t pedw = par[3] * par[6];
    for (n=0;n<=nmax;n++) {
      mean  = par[2] + n * par[3];
      p = x[0] - mean;
      if (n>0){
        sigma = (TMath::Sqrt(n)) * par[1];
      }
      else {
        sigma = pedw;
      }
      if (n>0){
        fu = fu + Poisson(n,par) * Gauss(1,p,sigma,par);
      }
      else {
        fu = fu + par[5] * Poisson(n,par) * Gauss(1,p,sigma,par);
```

```
        }
     }
     fu = par[4] * fu;
  }
  return fu;
}

Double_t Gauss(Double_t c,Double_t arg,Double_t sigma, Double_t *par)
{

  Double_t cons = 1/(TMath::Sqrt(2*TMath::Pi()));
  Double_t g = c*(cons/sigma)*TMath::Exp(-0.5*TMath::Power(arg,2)/
              TMath::Power(sigma,2));
  return g;
}

Double_t Poisson(int x, Double_t *par)
{

  return (TMath::Power(par[0],x))/Fac(x)*TMath::Exp(-(par[0]));
}

Double_t Fac(Double_t k)
{
  int i;
  Double_t f=1;
  for(i=1;i<=k;i++){
    f *=i;
  }
  return (f);
}
```

Appendix B

Hardware

CAEN 8 Channel Fast Amplifier, Mod. N412

CAEN Quad Linear Fan In - Fan Out, Mod. N401

CAEN Dual Delay, 3.5 ÷ 35 ns, Mod. N108 (2x)

CAEN Delay, 4 ÷ 67.5 ns, Mod. N107

CAEN 8 Channel Fast Discriminator, Mod. N413

CAEN Dual Timer, Mod. 2255B

CAEN Dual Timer, Mod. N93B (4x)

CAEN 3 Fold Logic Unit, Mod. N405 (2x)

DESY LED Driver, 0-100 mA, 1-100 kHz

LeCROY Linear Fan In - Fan Out, Mod. 428F

SEN Timer, Mod. Th277

LeCROY Coincidence Unit, Mod. 465

CAEN Quad Scalar an Preset Counter Timer, Mod. N145

CAEN 8 Channel Charge Integrating ADC, Mod. V265

MOTOROLA MVME - Processor, 162-043 + MVME 712/M

LeCROY 8 Channel TDC, Mod. 2228

CAEN 40 Channel High Voltage System, Mod. SY 127

CES A2 Crate Controller

TEKTRONIX Four Channel Digitizing Oscilloscope, Mod. TDS 540

CAMAC-, VME-, NIM-Crates
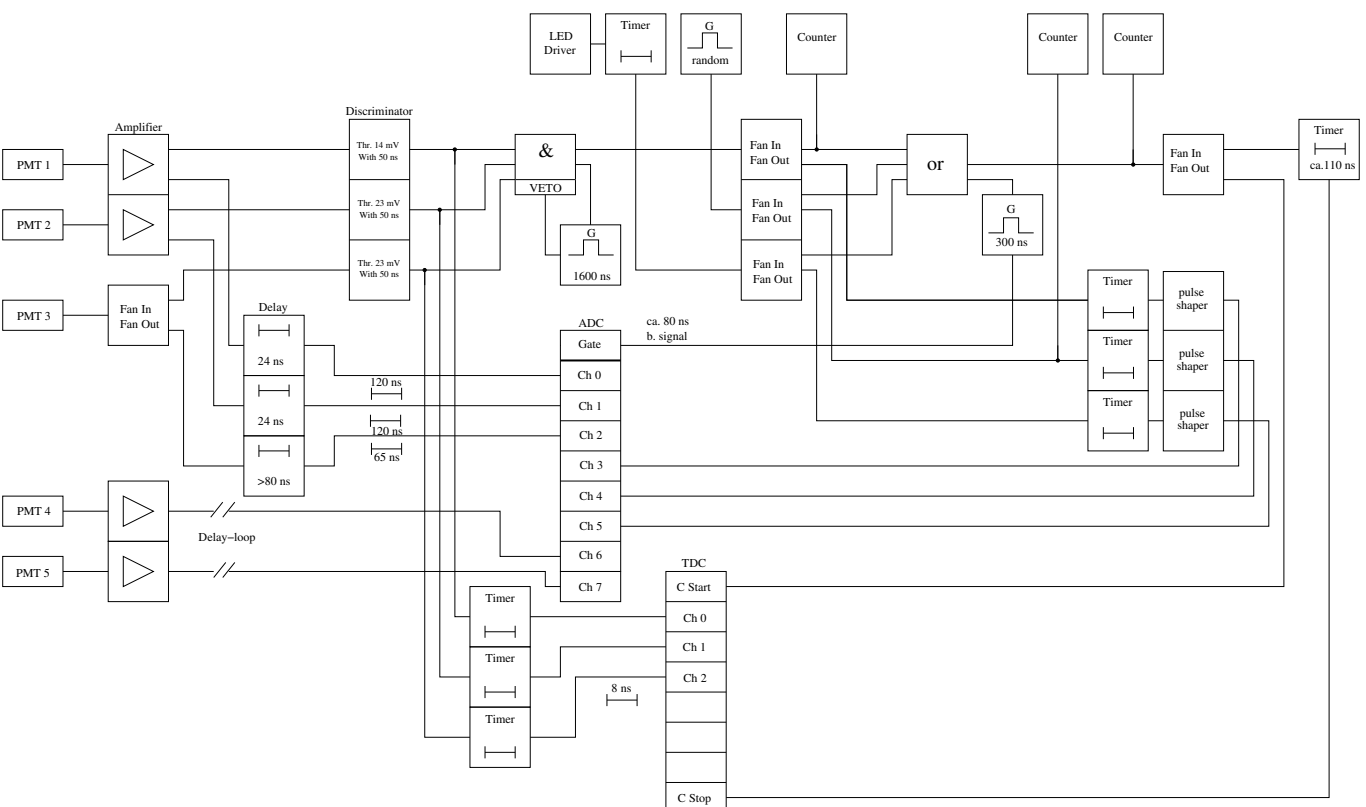
Figure B.1: *Variation of the experimental setup to measure the crosstalk with 3 photo multipliers.*
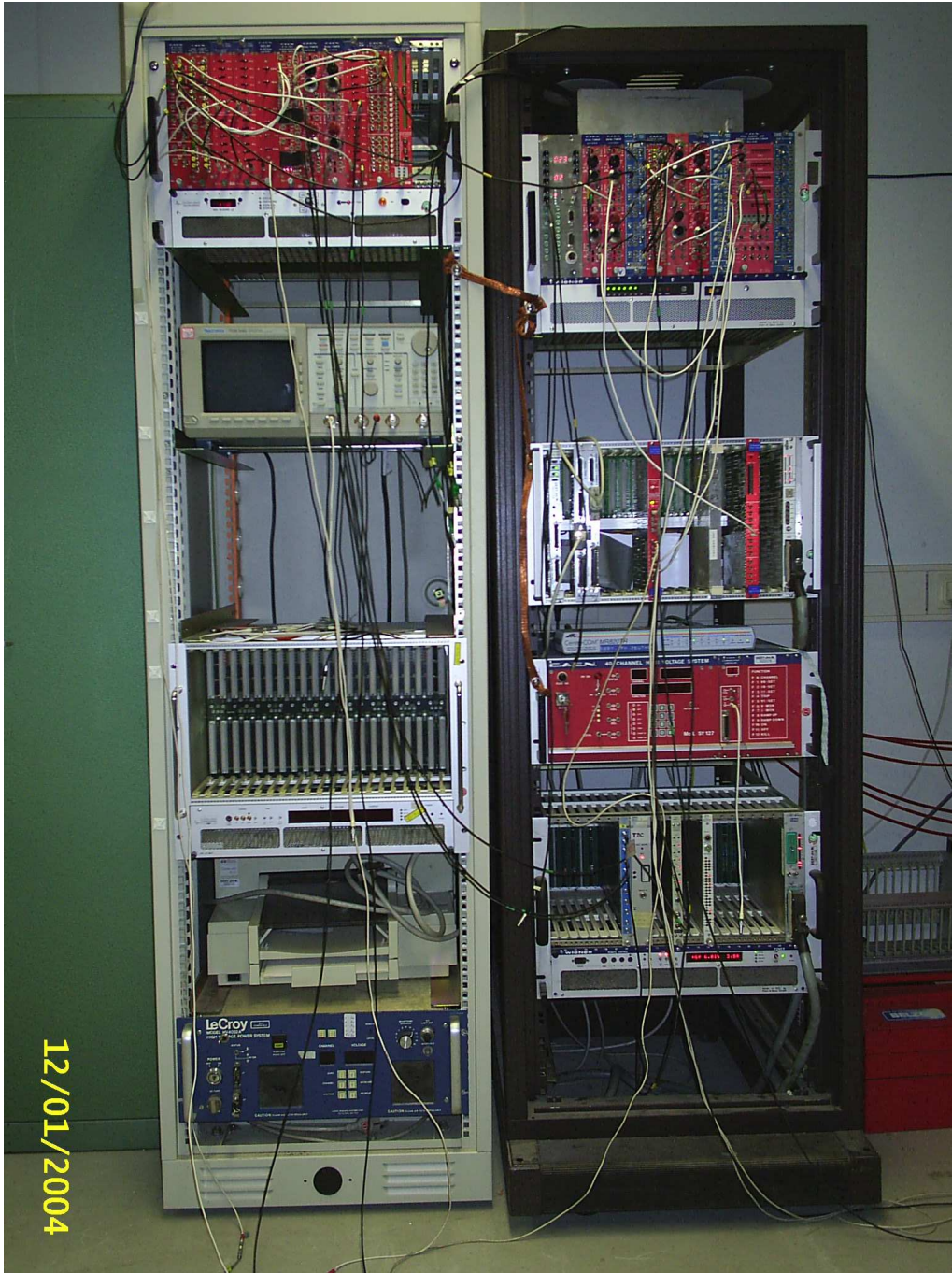
Figure B.2: *The Electronics.*
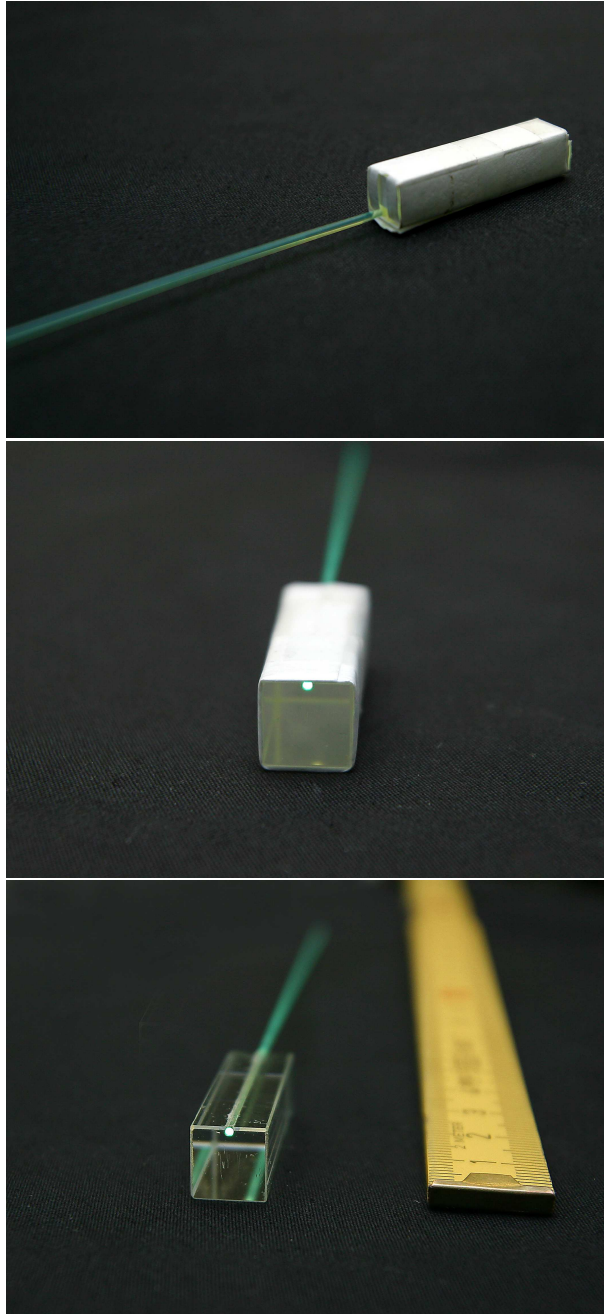
Figure B.3: *BC-408 (upper picture) and the lead glass sample.*
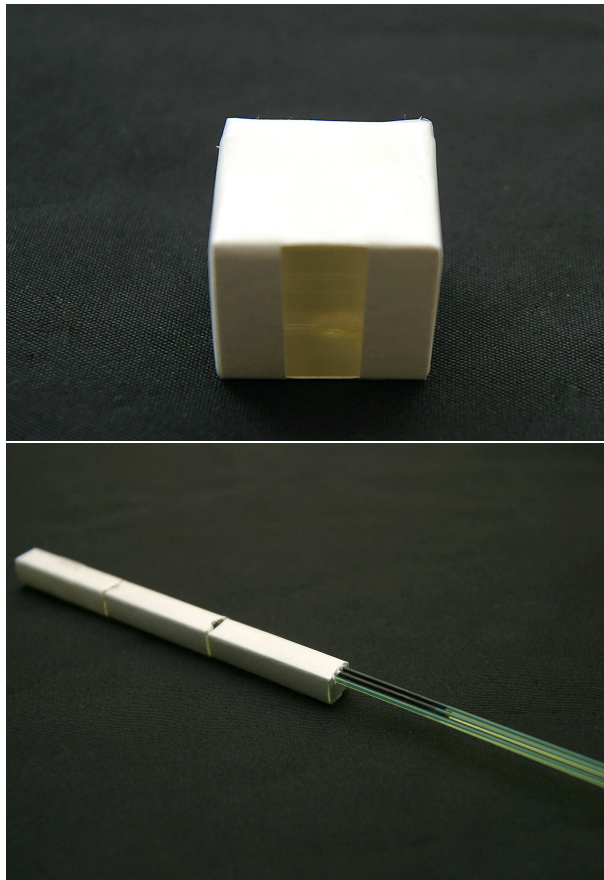
Figure B.4: *NaBi(WO₄)₂ sample and the 3x-sample.*

Appendix C

Calibration Curves
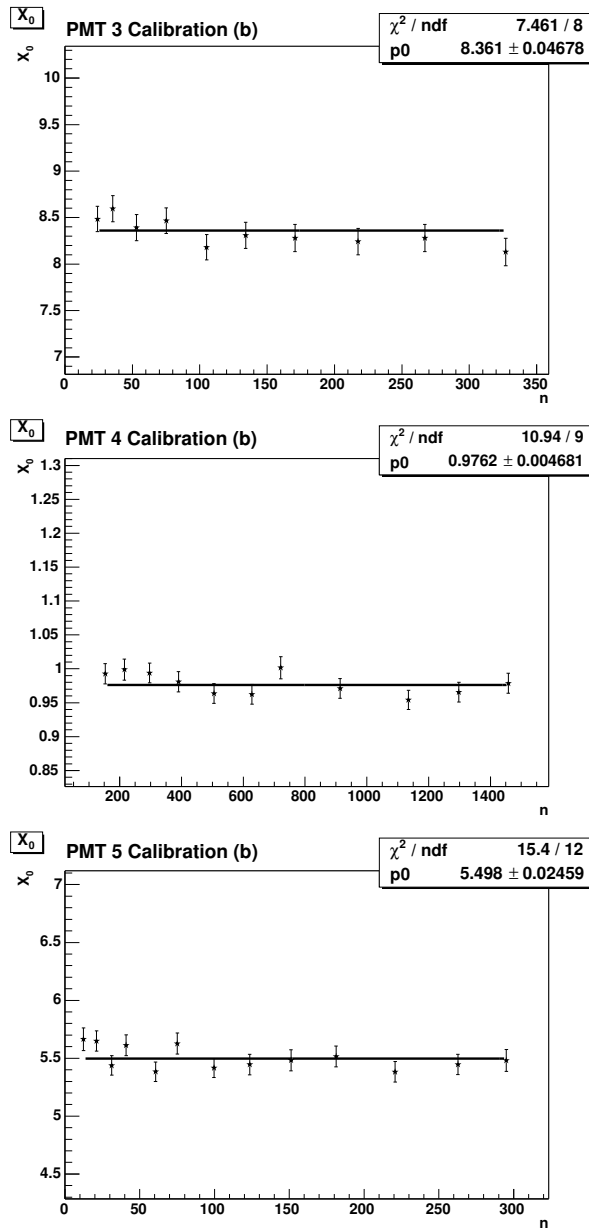
Figure C.1: *Recalibration of PMT 3,4,5 - Calibration (b).*
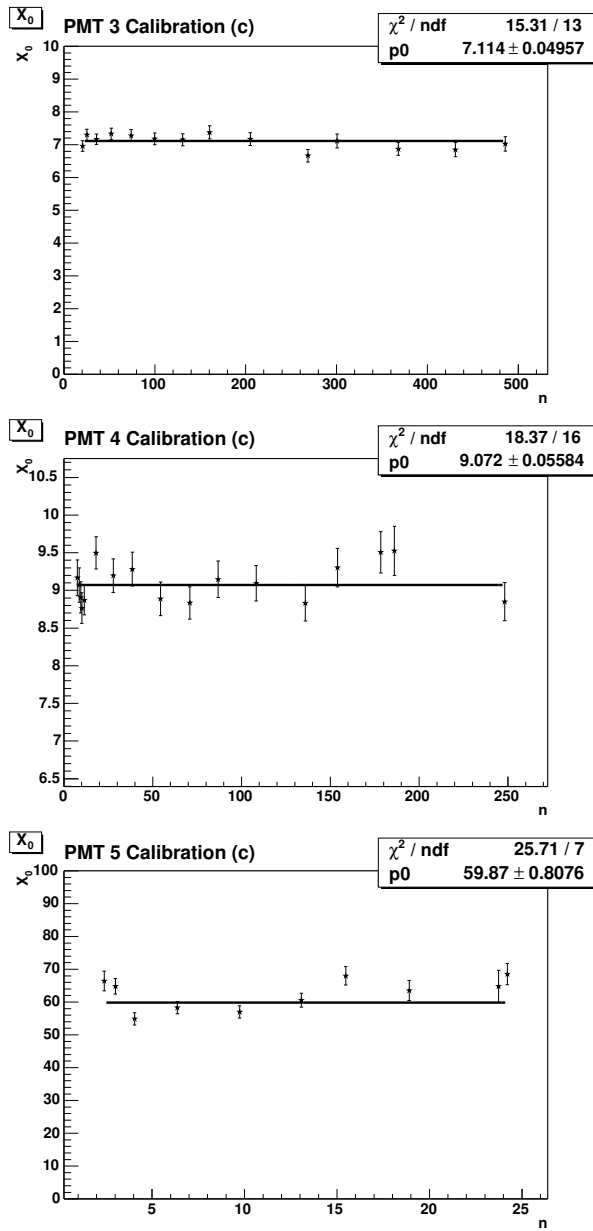
Figure C.2: *Recalibration of PMT 3,4,5 - Calibration (c).*

Bibliography

[1] S.P. Ahlen, "Theoretical and experimental aspects of the energy loss of relativistic heavily ionizing particles*", Rev. Mod. Phys. **52**, 121 (1980).

[2] S.P. Ahlen, "Calculation of the relativistic Bloch correction to stopping power", Phys. Rev. **A25**, 1856 (1982).

[3] W.-J. Becker, K.W. Bonfig, K. Höing, *Handbuch elektrische Meßtechnik*, (Hüthing, Heidelberg 1998).

[4] CAEN MOD. V 265 8 Channel Charge Integrating ADC, Technical Information Manual, Revision n. 1.; http://www.caen.it/nuclear/product.php?mod=V265

[5] CAEN - Costruzioni Apparecchiature Elettroniche Nucleari: http://www.caen.it/

[6] D.S. Gemmell, "Channeling and related effects in the motion of charged particles through crystals*", Rev. Mod. Phys. **46**, 129 (1974).

[7] D.E. Groom *et al*, "Muon stopping-power and range tables, 10 MeV–100 TeV", Atomic Data and Nuclear Data Tables **78**, 183-356 (2001).

[8] C. Grupen, *Teilchendetektoren*, (BI-Wiss.-Verl., Mannheim, Leipzig, Wien, Zürich 1993).

[9] HAMAMATSU Manual and final test sheet: Metal Package Photomultiplier Tube R7400U Series, HAMAMATSU PHOTONICS K.K., Electron Tube Center.

[10] HAMAMATSU PHOTONICS K.K.: http://www.hamamatsu.com

[11] H.V. Klapdor-Kleingrothaus/A. Staudt *Teilchenphysik ohne Beschleuniger*, (Teubner, Stuttgart 1995).

[12] LabVIEW: http://www.ni.com/labview/

[13] LeCROY 8 Channel TDC, Mod. 2228 Technical Data Sheet.

[14] LeCROY Corporation: http://www.lecroy.com/

[15] W.R. Leo, *Techniques for Nuclear and Particle Physics Experiments*, (Springer-Verlag, Berlin, Heidelberg 1987, 1994).

[16] W. Lohmann, "ENERGY LOSS OF MUONS IN THE ENERGY RANGE 1-10000 GeV", CERN **85-03**,(1985).

[17] K. Mitsui, "Muon energy-loss distribution and its applications to muon energy determinations", Phys. Rev. **D45**, 3051 (1992).

[18] Particle Data Group: http://pdg.lbl.gov/

[19] PAW Physic Analysis Workstation: http://wwwasd.web.cern.ch/wwwasd/paw/

[20] PHOTONIS Photomultiplier tubes, Technical Manual 2000.

[21] PHOTONIS imaging sensors: http://www.photonis.com

[22] R & D for the TESLA-Detector: Instrumentation of the very forward region, The Forward Calorimeter Group, December 2002.

[23] ROOT, An Object-Oriented Data Analysis Framework: http://root.cern.ch/root/Welcome.html

[24] Saint-Gobain CRYSTALS and DETECTORS: http://www.bicron.com

[25] W.K. Sakumoto *et al*, "Measurement of TeV muon energy loss in iron", Phys. Rev. **D45**, 3042 (1992).

[26] SCHOTT GLAS Optics for Devices, Optisches Glas Taschenkatalog 2003, V1.5 März 2003.

[27] SCHOTT GLAS, Mainz: http://www.schott.com

[28] R.M. Sternheimer *et al*, "Density effect for the ionisation loss of charged particles in various substances", Phys. Rev. **B26**, 6067 (1982).

[29] R.M. Sternheimer *et al*, "General Expression for the Density Effect for the Ionisation Loss of Charged Particles*", Phys. Rev. **B3**, 3681-3692 (1971).

[30] R.M. Sternheimer, "The Density Effect for the Ionization Loss in Various Materials*", Phys. Rev. **88**, 851 (1952).

[31] R.M. Sternheimer, "The Energy Loss of a Fast Charged Particle By Čerenkov Radiation*", Phys. Rev. **91**, 256 (1953).

[32] R.M. Sternheimer *et al*, "DENSITY EFFECT FOR THE IONISATION LOSS OF CHARGED PARTICLES IN VARIOUS SUBSTANCES", BNL **33571**, (1953).

[33] TESLA Technical Design Report, DESY 2001-011, ECFA 2001-209, March 2001.

[34] http://www.tektronix.com/

[35] R. Wigmans, Calorimetry - *Energy Measurements in Particle Physics*, Clarendon Press, Oxford, 2000.

Acknowledgments

Erklärung

Hiermit bestätige ich, daß ich die vorliegende Arbeit ohne unerlaubte fremde Hilfe angefertigt habe.
Mit der Auslage meiner Diplomarbeit in der Bibliothek der Humboldt–Universität zu Berlin bin ich einverstanden.

Berlin, den 06. Februar 2004

Ralph Dollan